An investigation of Ca_3CoMnO_6 as a thin-film layer on oxide thermoelectric materials

Andreas Connor Olofsson

Thesis for the degree of Master of Science submitted to the Faculty of Mathematics and Natural Sciences

Department of Chemistry
University of Oslo

15.06.2020

Abstract

Thermoelectric generators (TEG) have been a long established, mature technology for energy conversion of heat into electricity. Traditional TEGs are often comprised of expensive or rare elements to achieve high efficiency, however this sets limitations on the operating temperatures, and large-scale applications. In this context, oxide thermoelectric materials have become widely studied after the discovery of the high performing oxide, Na_xCoO_2.

$CaMnO_3$ and $Ca_3Co_4O_9$, assembled as a thermoelectric generator with a direct p-n junction, saw the formation of a coexisting $Ca_3Co_{2-x}Mn_xO_6$ phase at the junction when operated at high temperatures. Due to the increased power output of the module compared to similar devices, investigations of the reaction phase $Ca_3Co_{2-x}Mn_xO_6$ was undertaken. However, not all of its properties are fully understood. The goal of this project has been to investigate such a device and try to bring more clarity into its operating properties.

Samples of each material component was synthesised and characterized, to investigate defect chemistry, conductivity and their thermoelectric properties. They were then put in a larger context by investigating the fundamental properties of the p-n junction formed between them.

Thin films of $Ca_3Co_{2-x}Mn_xO_6$ were synthesised by Pulsed Laser Deposition (PLD) and found to give homogeneous growth on both Al_2O_3 and on $CaMnO_3$, with thicknesses of around 500 nm and 750 nm for the 10 k and 20 k shots respectively on Al_2O_3. When placed between the two bulk materials, $CaMnO_3$ and $Ca_3Co_4O_9$, the coexisting properties of $Ca_3Co_{2-x}Mn_xO_6$ is shown to improve the junction between them, by acting as an intermediate layer helping the conductivity and therefor efficiency of the module.

All investigations into the individual thermoelectric properties of the materials showed a generally lower conductivity and Seebeck coefficient compared to literature values for all materials. $CaMnO_3$ showed a conductivity of 32 S cm^{-1} and Seebeck coefficient of -200 µV K^{-1}, $Ca_3Co_4O_9$ showed a conductivity of 63 S cm^{-1} and a Seebeck coefficient of 135 µV K^{-1} and Ca_3CoMnO_6 showed a conductivity of 0.01 S cm^{-1} and Seebeck coefficient of 300 µV K^{-1} at temperatures of 800 °C

The reaction between $CaMnO_3$ and $Ca_3Co_4O_9$ was expected, creating the $Ca_3Co_{2-x}Mn_xO_6$ interlayer when joined at high temperatures. Measurements of the junction showed increased resistance as the thickness of the layer grew. For the $CaMnO_3$-$Ca_3Co_4O_9$ junction with the

thin-film layers, the p-n junction behaved also as expected, as the coexisting thin-film layer hindered the reaction between $CaMnO_3$ and $Ca_3Co_4O_9$

Further work should be conducted, however, since the wide arrangement of different compositions for the $Ca_3Co_{2-x}Mn_xO_6$ interlayer should be optimised in the junction between $CaMnO_3$ and Ca_3Co_4O.

Preface

This thesis is submitted as part of the masters degree in Material Science and Nanotechnology by the Department of Chemistry at the University of Oslo. The work was carried out in the Group of Electrochemistry from August 2018 to June 2020.

The work presented in this thesis would not be possible without a squad of imperative people. First, I would like to say big thanks the Group of Electrochemistry at the University of Oslo, and the scientific community that has surrounded me these last years, it has been a true privilege to work and study in your presence. I would also like to grant the largest of thanks to my supervisor Prof. Truls Norby, and my co supervisors Raphael Schuler and Nikola Kanas for their time, patience and discussions, whom without this work would not have been possible. I would also like to thank Xiaolan Kang for the help with the SEM and analysis of the results, Amir Masoud Dayaghi for the help with the PLD and fruitful advice along the way, and Salah Bra Amedi for the help with the XRD. I would also extend the greatest gratitude to my fellow master students, especially Visa, Hege and Jónína, whom I have had the pleasure of sharing an office with during the duration of this work.

Second, I would like to thank all the friends I have gotten, and inspiring people I have met during my five years at the University of Oslo, the studies would not have been the same without you. In addition, a special thanks my flatmates Erlend and Kristian, as well as the whole top floor of Bjølsen H08, making life as enjoyable off campus as on it.

Last, I would like to thank my family for their overwhelming support and encouragement during my time at University. The Sunday dinners were a welcoming breath of fresh air, and an often-awaited occurrence. Again, my greatest thanks to all the individuals that I have become acquainted to, since there is far too many to name them all.

Oslo. 15th of June, 2020

Andreas Connor Olofsson

List of Abbreviations

TEG	Thermoelectric Generator
CCMO	Ca_3CoMnO_6
CCO	$Ca_3Co_4O_9$
CMO	$CaMnO_3$
PLD	Pulsed Layered Deposition
SEM	Scanning Electron Microscopy
XRD	X-ray Diffraction
ETD	Everhart-Thornley Detector
SSD	Solid-State Detector

Contents

1 Introduction

With climate change and global warming becoming one of the biggest challenges in the 21st century [1, 2], the implementation of additional renewable energy sources has become vital to gradually reduce the use of fossil fuels and tackle global climate change associated with global warming. Energy from the direct conversion of heat to electrical energy is possible with the use of thermoelectric generators or TEGs. A major benefit of TEGs is that they don't contain any moving parts or involve any chemical reactants, they operate solely on thermodynamics. However TEGs suffer from low conversion efficiency of heat to electricity, and together with the high production cost of efficient devices TEGs are not widely utilized. Recently the use of TEGs in applications for heat recovery has gained traction with the discovery of new materials such as oxides and alloys, having lower capital costs and higher temperature stability. TEGs are being implemented in vehicles and industry to exploit the waste heat from existing systems [3, 4]. With ongoing research into thermoelectric materials and the implementation of these materials into modules, TEGs could help utilize the energy currently being lost as waste heat and provide energy efficient systems for our society.

1.1 Thermoelectric Materials

Thermoelectric materials are materials that exhibit the thermoelectric effect, a phenomenon where a temperature difference across a sample creates an electric potential, or a potential difference across a sample will create a temperature difference [5]. The driving force for these processes can be explained by the three reversible effects, the Seebeck, Peltier and Thomson effect, where the Thomson effect relates the first two together. Non-reversible effects are also present with the movement of charges and heat in materials, for example Joule heating, heating caused by resistance in the material and thermal conduction caused by the flow of heat in a temperature gradient.

1.1.1 Seebeck Effect

In 1821 Thomas Seebeck discovered the presence of an electric current when two dissimilar conductors were placed in a loop kept at different temperatures. This effect called the Seebeck effect will induce a potential difference in a thermoelectric material placed in a heat gradient. The free charge carriers of the material will then diffuse towards the colder end of the material, creating the potential difference across the sample, Figure 1-1.

Figure 1-1: Illustration of the potential build-up as result of the Seebeck-effect. Electrons shown in blue migrating from the hot side (left) to the cold side (right)

The potential created as a result of the temperature gradient is material specific and can be expressed by the following equation (Eq. 1.1)

$$S = \frac{\Delta U}{\Delta T} \qquad \textit{Eq. 1.1}$$

here ΔU is the voltage difference, ΔT is the temperature difference, and S is the Seebeck coefficient of the material.

1.1.2 Peltier Effect

When current is passed through two different conductors there will be a change in temperature at the junction. This is known as the Peltier effect, after Jean Charles Athanase Peltier who discovered it in 1835. The exchange of heat comes from the change in the entropy of the charge species, having crossed the junction, making the direction of the current responsible for heat being absorbed or emitted at the junction. It can be expressed as

$$\Delta Q = \Pi I \qquad \textit{Eq. 1.2}$$

where ΔQ is the amount of heat, Π is the Peltier coefficient and I is the current flowing through the conductor. The heat generated can often be accompanied by other heating effects such as Joule heating prominent in metal conductors.

1.1.3 Thomson Effect

The last thermoelectric effect is the Thomson effect. Observed in 1851 by Lord Kelvin, it explains the emission or absorption of heat when current is flowing through a conductor placed in a temperature gradient. The heat rejected or absorbed is given by the equation ()

$$\Delta Q = -\beta I \Delta T \qquad \textit{Eq. 1.3}$$

where β is the Thomson coefficient, I is the current and ΔT is the temperature difference. Thomson also related the Peltier effect to the Seebeck effect through temperature giving rise to the relationship

$$\Pi = S\,T \qquad \textit{Eq. 1.4}$$

1.2 Thermoelectric Modules

Thermoelectric modules utilize the Seebeck and Peltier effects explained above to covert heat into an electric current or vice versa. Such devices often consist of a n-type and p-type thermoelectric material connected together with a conducting material, often comprising of noble metals [3, 6]. The voltage produced from one such module is low, so multiple modules are connected electrically in series and thermally in parallel and form a thermoelectric generator capable of producing sufficient current or cooling.

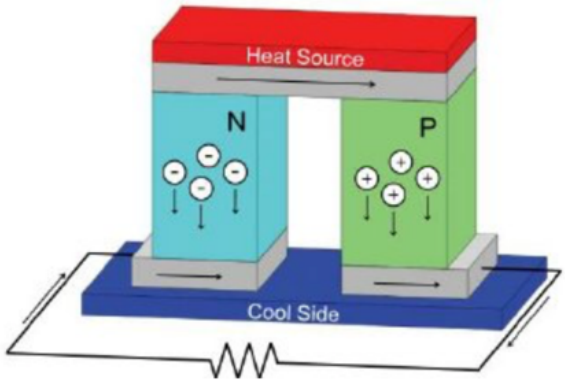

Figure 1-2: Thermoelectric module working as a heat generator [7].

1.3 Types of Modules

Leg-modules as depicted in Figure 1-2, are the most common type of modules in TEGs and consist of two legs of opposite thermoelectric material (Figure 1-2) and are mainly used as Peltier devices for cooling applications. However, in order to improve the efficiency of TEGs, different architectures are being investigated such as thin-film based structures, chains of a single n-type or p-type thermoelectric material, pyramid shaped devices with multiple thermoelectric modules stacked on top of each other and TEGs with a direct contact between the n-type and p-type material [8-11]. Efficiency of TEGs is however a very complex system, since it not only depends on the efficiency of the thermoelectric materials used, but is affected by the losses attributed to the contacts between the thermoelectric material and the interconnects. One such example is the improvement of power output by around 70% when the legs of the thermoelectric material was changed from a cuboid structure to a pyramid structure [10].

At elevated temperatures the contact between the thermoelectric material and metallic interconnect becomes an issue, with mechanical stress due to mismatch in thermal expansion, diffusion of atoms between the interfaces and chemical instability. Becker *et al.*[12] showed that the replacement of the interconnects with a p-n junction was possible, generating electron-hole pairs from the space charge region. Kogo *et al.[13]* recently demonstrated increased energy harvest and cooling of a TEG with a p-n junction, Figure

1-3, compared to a TEG with metal interconnects between the p and n-type material on both sides.

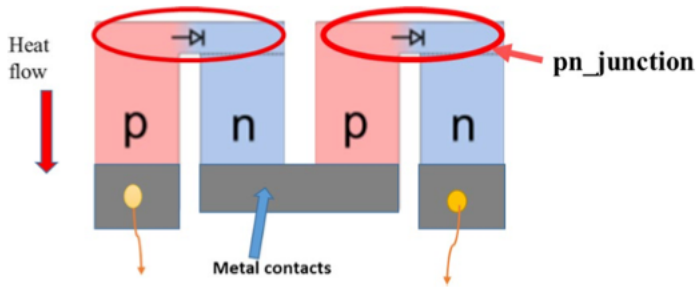

Figure 1-3: Thermoelectric generator with a direct p-n junction on the hot side of the module.[13]

1.3.1 Efficiency of Thermoelectric Modules

The efficiency of thermoelectric modules when in power generation mode can be shown to be [14].

$$\epsilon = \left(\frac{T_H + T_C}{T_H}\right)\frac{\left(\sqrt{1+ZT}-1\right)}{\sqrt{1+ZT}-(T_C/T_H)} \qquad \textit{Eq. 1.5}$$

where T_C and T_H are the respective cold and hot ends of the temperature gradient, and ZT is the figure-of-merit for the module as a whole. The first term in the equation represents the Carnot-efficiency since the generator is in all aspects a type of heat-engine. Improving the efficiency does not only depend on a good figure-of-merit for the module, but also having a high temperature difference between the cold and hot end [15].

1.4 Figure of merit

The basis for comparing thermoelectric materials is the figure-of-merit zT, containing the Seebeck coefficient (S), electrical conductivity (σ) and thermal conductivity (κ)

$$zT = \frac{S^2 \sigma T}{\kappa_e + \kappa_l} \qquad \textit{Eq. 1.6}$$

With the thermal conductivity expressed as the transport contributions from both lattice vibrations (κ_l) and the heat transport of the charge carriers (κ_e). A figure-of-merit of around one is usually considered to be an efficient thermoelectric material [3], although it only corresponds to an Carnot efficiency of around 10%. From the equation (Eq. 1.6) high zT values are obtained when materials have high Seebeck coefficient and electrical conductivity, but low thermal conductivity. These three properties are however correlated, so when trying to enhance one of them the others will often be affected in a negative manner[6]. The Wiedemann-Franz law directly links the electrical conductivity to the thermal carrier conductivity [16] and can be further liked to mobility by

$$\kappa_e = \sigma LT = zcuLT \qquad \textit{Eq. 1.7}$$

where L is the Lorenz number. Often the Lorenz number is taken to be constant, but has been shown to vary with temperature, carrier concentration and scattering effects [17].

The typical way to improve the values of these material properties is to dope the thermoelectric material, doing so increases the carrier concentration of the major charge carrier [14, 18]. The relation between the different contributions to achieve a high figure-of-merit is illustrated in Figure 1-4.

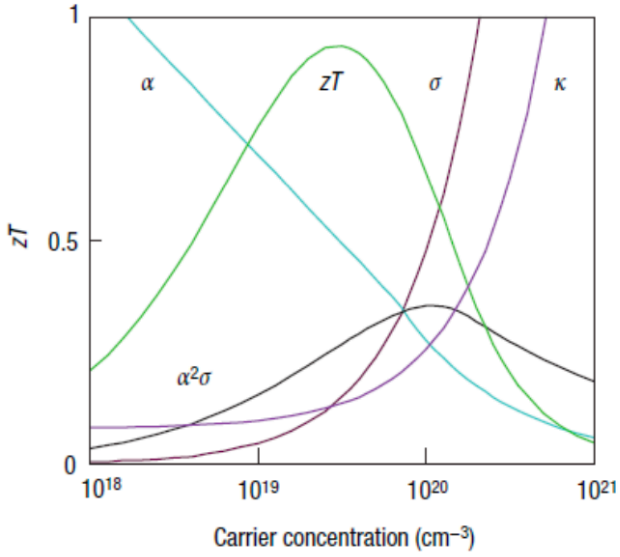

Figure 1-4: Carrier concentration effect on the Seebeck coefficient (α), electrical conductivity (σ) and thermal conductivity (κ). Trends shown are modelled after Bi_2Te_3, taken from [6]

1.5 Oxide Thermoelectric Materials

One way to increase the efficiency of modules is to have a large temperature gradient, or higher operating temperatures (Eq. 1.5). Traditional thermoelectric materials used in TEGs because of good thermoelectric properties, such as Bi_2Te_3, PbTe, SiGe, Sb_2Se_3 and Sb_2Te_3 have low durability at high temperatures, high fabrication cost and high toxicity making them undesirable in modules for high temperature. Research and calculations on possible new candidates for thermoelectric materials, has resulted in a multitude of different materials that are stable at elevated temperatures and could possible work in new modules to increase their efficiency [18, 19].

Oxides are materials with several combinations of elements and structure types, and are typically chemically stable at high temperatures, have low production costs, and more environmentally-friendly fabrication, than the rare elements used in very efficient devices (Figure 1-5). However, oxides generally suffer as materials with high zT due to their typical insulating properties with low electrical conductivity, and higher atomic vibration frequency as a result of lower average atomic mass, resulting in higher thermal conductivity. Optimal properties for any thermoelectric material are materials with

phonon-glass and electron-crystal properties [6], meaning low lattice thermal conductivity as in a glass and high electrical conductivity as in a crystal.

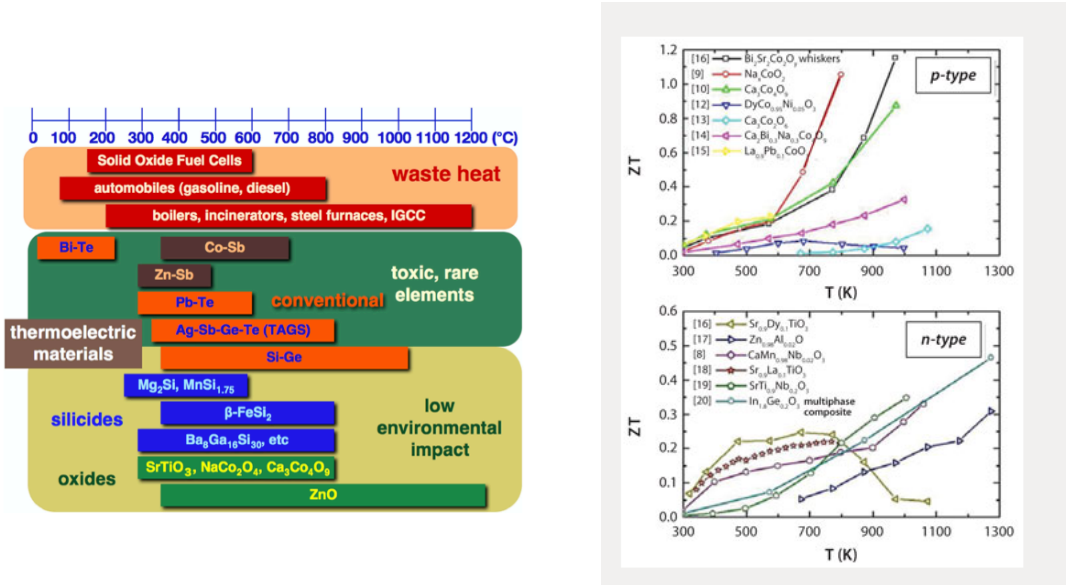

Figure 1-5: Operational temperature of various thermoelectric materials (left) and figure of merit (zT) for selected n-type and p-type oxides (right)[20]

Oxides started to become a real contender to traditional thermoelectric materials with the discovery of $NaCo_2O_4$ in 1997 by *Terasaki et al.*[21] The single crystal showed a surprisingly large thermopower of 100 μV/K, having metallic conductivity (0.2 mΩ cm) and Seebeck coefficient that did not follow the typical linear dependence, resulting in a zT of around one at intermediate temperatures. Other prominent oxide thermoelectric materials have since been discovered with best performing p-type oxides based on layered cobaltite systems [3, 18, 22].

For n-type oxides $SrTiO_3$ doped with an electron donor have been shown to have higher electrical and thermal conductivities than the cobaltites [3, 18]. $CaMnO_3$ is also considered a good n-type oxide, but with lower conductivities than $SrTiO_3$. $CaMnO_3$ is usually doped to increase its thermoelectric properties, and dopants on both the A- and B-site are common with typical dopants such as; La, Mo, Nb, Bi and Yb [18, 23, 24]. ZnO is also a strong candidate due to the simplicity of increasing conductivity by adding dopants such as Al, Sb and Mn, however, drawbacks of the material is a high thermal conductivity. The figure-of-merit of these oxides are still well beneath traditional thermoelectric materials, show in Figure 1-5

1.6 Research Aim

A recent publication by *Kanas et al*.[25], on an all-oxide thermoelectric module, showed the formation of a thin film reaction layer comprising of the stable product $Ca_3Co_{2-x}Mn_xO_6$ (CCMO), when the p-type $Ca_3Co_4O_9$ (CCO) and n-type $CaMnO_3$ (CMO) were operated in direct contact with each other. They observed an increase to unexpectedly large thermoelectric voltages, when an intended CCO-CMO thermoelectric single leg pair module was operated with a direct p-n-junction. They found that the coexisting phase of CCMO in contact with CCO and CMO was increasing the thermoelectric efficiency of the module.

Not all aspects of these results are understood or have rational plausible explanations, partly because the properties of CCMO are not extensively mapped and because the properties and behaviour of oxide p-n-junctions have not been fully explored, particularly not at high temperatures or for thermodynamically stable couples such as ZnO and NiO, or unstable couples such as CCO and CMO.

The main aim of this thesis is to expand the understanding of the processes taking place when operating the CCO-CMO as a direct contact thermoelectric module. All three compounds, CCO, CMO and CCMO will be investigated individually characterizing their structure and electrical properties. Thin-films of CCMO will also be created on CMO to investigate and compare the effect of CCMO that has been grown as a result of CCO-CMO reacting, and the CCMO thin-films in-between CCO and CMO. Since the growth of CCMO creates a dense, cobalt-rich, calcium-deficient layer at the interface, the CCMO thin-films will create a smoother transition between the three compounds.

2 Theory

2.1 Electrical Conductivity

Electrical conductivity of materials depends on the transport of electrical charge species, either ionic charge carriers or electronic charge carriers or both depending on the material. Electronic charge carriers, electrons and holes often have higher mobility and dominate the conductivity, influenced by their ability to flow in a specific direction under the influence of an electric field. The flow is limited by scattering events, when the carriers scatter off lattice vibrations (phonons), defects and impurities.

An electrical field, E will impress a force, F on any species, i with a charge, $z_i e$. This force is proportional to the strength of the electrical field and the charge of the species,

$$F = z_i e E \qquad \textit{Eq. 2.1}$$

The flux density of particles, j_i will therefore be proportional to the force, since the flux is the product of the charge carrier concentration, c and their drift velocity, v. Substituting the velocity with the mechanical mobility, B_i and the force acting, F we get

$$j_i = F c_i B_i \qquad \textit{Eq. 2.2}$$

Current density, i_i of the species, i is the product of the flux density and charge, and introducing the charge mobility as $\mu_i = |z_i| e B_i$ they can be related in the fashion

$$i_i = z_i e F c_i B_i = F c_i \mu_i = c_i \mu_i z_i e E = \sigma_i E \qquad \textit{Eq. 2.3}$$

The conductivity of the material will then be the total sum of all of the partial conductivities, σ_i present in the material. For electrons the conductivity and mobility can

then be related with $\sigma = ne\mu$ where n is the concentration of electrons, and similarly for holes.

2.1.1 Transport in Polar Solids

When electrons and holes move in polar compounds, solids with ionic character to their bonding, the charge carriers will interact with the crystal lattice as it moves, causing local deformations (Figure 2-1). The electron-phonon interaction can be treated as a quasi-particle, or a polaron. With weak electron-phonon interactions the polaron is called a large polaron and treated as an electron with a larger effective mass due to the localized deformation it carries with it. If the interaction is strong, the potential created by the deformation may trap the carrier. The charge carrier needs extra energy to move from the localized site, and the electronic transport occurs via thermally activated hopping processes between localised states.

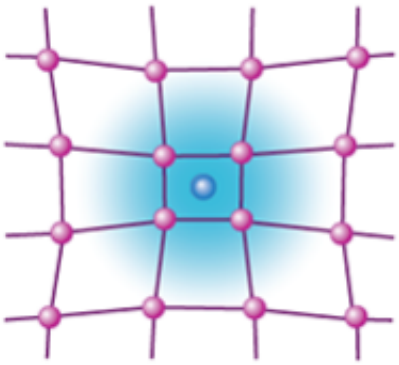

Figure 2-1: Illustration of a polaron in a lattice crystal. The electron interacts with the surrounding lattice and distorts the atom positions as it moves through the crystal. Taken from [26]

The mobility can then be related to the conductivity through the Nernst-Einstein equation.

$$D_i = u_i \frac{k_B T}{z_i e} = \sigma_i \frac{k_B T}{c_i z_i^2 e^2} \qquad \textit{Eq. 2.4}$$

where D_i is the self-diffusion coefficient, k_B is the Boltzmann constant and T the absolute temperature in Kelvin. The mobility of the carriers can then be expressed as

$$\mu = \frac{\mu_0}{T} \exp\left(-\frac{E_a}{k_B T}\right) \qquad \textit{Eq. 2.5}$$

where E_a is the activation energy for the hopping mechanism. Arrhenius plots of $\ln(\sigma_i T)$ vs $\frac{1}{T}$ will yield a straight-line relationship, with information about the conductivity in the material, and the activation energy can be found as it corresponds to the slope of the straight line, while the intercept of the y-axis is equal to $\ln(\mu_0)$

2.2 Seebeck Coefficient

As indicated before the three thermoelectric effects, Seebeck, Peltier and Thomson express the relation between the flow of heat and electric current, their coefficients related through the Kelvin relations.

The Seebeck coefficient can be explained as the voltage build up when a small temperature gradient is applied to a material. Charge carriers will have higher kinetic energy in the hot region of a material compared to the cold region. Higher kinetic energy results in higher velocity of the charge carriers, and results in a net diffusion of charge carriers towards the cold region of the material. This diffusion will create a voltage difference between the two regions, and after equilibrium has been achieved a potential will exist between the two ends. Phonon drag will also occur, where the interaction between the electrons and holes, and the phonons are strong. This extra effective mass due to the phonon-electron/hole interaction will add to the existing potential. Phonon drag is however highly temperature dependant, because at low temperatures the amount of phonons is low, and at high temperatures the phonons lose their momentum by scattering off each other, instead of with electrons [16].

One can estimate the Seebeck coefficient in semiconductors to a degree using simple assumptions of weak electron-electron interaction and weak phonon-electron interaction. Seebeck coefficients for electrons and holes can then be expressed as,

$$\alpha_e = -\left(\frac{k_B}{e}\right)\left[\frac{5}{2} - \ln\left(\frac{N_c}{n}\right) + K_e\right] \qquad \textit{Eq. 2.6}$$

$$\alpha_h = \left(\frac{k_B}{e}\right)\left[\frac{5}{2} - \ln\left(\frac{N_v}{p}\right) + K_h\right] \quad \textit{Eq. 2.7}$$

here Nc and Nv represent the density of states of the conduction band and valence band respectfully, k_B is the Boltzmann constant, n and p are the concentration of electrons and holes while K_e and K_h are correction terms to account for thermal collisions and other scattering events [27]. This can be expressed with the fermi level, by substituting in the expressions for concentration of electrons in the conduction band, and holes in the valence band and ignoring the correction terms

$$n = N_C \exp\left(\frac{E_F - E_c}{k_B T}\right) \quad \textit{Eq. 2.8}$$

$$p = N_V \exp\left(\frac{E_V - E_F}{k_B T}\right) \quad \textit{Eq. 2.9}$$

inserting Eq. 2.8 and Eq. 2.9 into the equations for Seebeck (Eq. 2.6 and Eq. 2.7) we have

$$\alpha_e = -\left(\frac{k_B}{e}\right)\left[\frac{5}{2} - \left(\frac{E_F - E_C}{k_B T}\right)\right] \quad \textit{Eq. 2.10}$$

$$\alpha_h = \left(\frac{k_B}{e}\right)\left[\frac{5}{2} - \left(\frac{E_V - E_F}{k_B T}\right)\right] \quad \textit{Eq. 2.11}$$

The sign of the Seebeck coefficient tells what kind of dominant charge carrier is present, and therefor if the material is n-type or p-type. The concentration of charge carries in the material will impact the absolute Seebeck coefficient, and a large concentration of electrons or holes will result in a low Seebeck coefficient. For semiconductors at high temperatures the entropy of the system can be explained by the classical Boltzmann formula, and Heikes formula can be calculated [6].

$$\alpha = -\frac{k_B}{e}\ln\left(\frac{1-c}{c}\right) \quad \textit{Eq. 2.12}$$

here c is the fraction of defects or equivalently the mobile charge carriers.

2.3 Defect Chemistry

Crystalline materials have a highly ordered microscopic structure, where atoms sit in specific lattice sites that repeat indefinitely in all directions of the crystal. However, when the temperature is above 0 K defects will be present in the structure. The functional and mechanical properties of materials are highly influenced by the presence of these defects. This is because of all the lattice sites being occupied in the perfect crystal structure, and as a result there is no transport between the sites.

Defects allow atoms, ions and electrons to move in the structure since the perfect crystal lattice is not so perfect anymore, and also allows for diffusion throughout the material. Incorporation of defects into structures has therefor become extremely important to tune material properties, since defects are the main transport mechanism of ions and atoms in solids. Defects are differentiated in two main groups; structural- and electronic defects. Structural defects are also differentiated in subclasses depending on their dimensionality.

Zero-dimensional: These defects are limited to a single lattice site and are called point defects. Point defects can be vacancies, interstitials, substitutions and electronic defects. Electronic defects are however generally made from internal excitation and have the possibility to move much more freely in the crystal.

One-dimensional: Dislocations in the lattice caused by line and plane defects that shift the lattice in a certain direction.

Two-dimensional: Shifts in multiple directions cause defects such as stacking faults, grain boundaries or surfaces. Grain boundaries are expected to be present in $CaMnO_3$, $Ca_3Co_4O_9$ and Ca_3CoMnO_6.

Three-dimensional: Shifts in all three lattice directions cause volume or bulk defects. These can be cracks, precipitations or inclusions of foreign substances. In CMO, CCO and CCMO these could appear when two different phases are present beside each other. The interfaces between CMO/CCO and CCMO is also expected to have such defects.

Defect reactions can be written in the same way as chemical reactions as long as the three laws of conservation are met.

1. Conservation of mass
2. Conservation of charge
3. Conservation of the ratio of structure sites

In other words, the total number of atoms must be the same before and after the reaction, the charge before and after the reaction must be equal, as they should remain electrically neutral and the ration of anion to cation must be constant. This also implies that when new defects are formed in a structure, they need to be compensated by other defects such as vacancies, interstitials and electronic defects.

There are several different defect notations that have been proposed and used in chemistry, but the one used in this thesis will be the Kröger-Vink notation. The general defect notation is A_S^c where A is the chemical species, c is the effective charge of the species and s is the site relative to the original structure. The effective charge of a species is calculated by taking the charge on the current site and subtracting the charge on the original site. Charges are denoted "•" for positive, "/" for negative and "x" for neutral. For vacancies and interstitials, "v" and "i" are used instead of the chemical symbol and the related structure site respectively.

2.4 Semiconductors

Semiconductors are a group of materials having electrical conductivities intermediate between conductors such as metals and insulators such as rubber. The conductivity of these materials can be varied over orders of magnitude by changes in temperature, the amount of impurities and optical excitation. The simplified band scheme of metals, insulators and semiconductors is shown in Figure 2-2 The valence band is filled, and the conduction band is empty with an energy gap between E_{Gap}. For metals there is no energy gap, but the valence band and conduction band overlap.

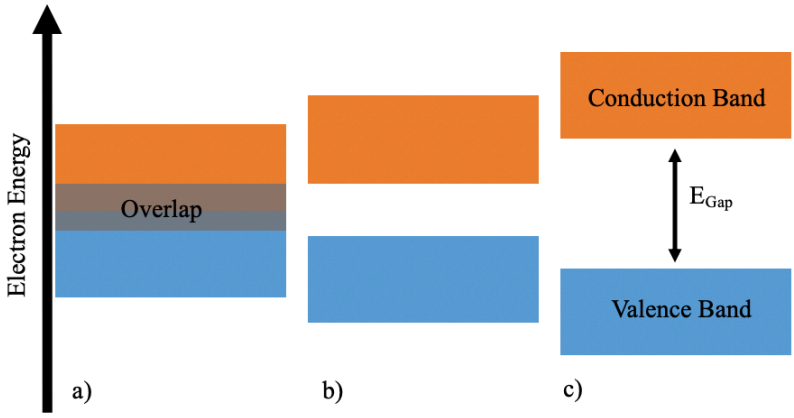

Figure 2-2: Simplified band structure of a metal (a), semiconductor (b) and insulator (c). The valence band is filled with electrons and the conduction band is empty. For semiconductors and insulators, the electrons have to cross the band gap to get from the valence band and into the conduction band.

Electrons in the valence band, can be thermally excited to the conduction band to create an electron-hole pair. The empty states in the valence band are called holes and contribute to the conductivity together with the electrons. A perfect semiconductor crystal with no impurities or lattice defects is called an intrinsic semiconductor and the charge carries are only created by thermal excitation. To increase the number of charge carriers in a material, impurities are introduced creating extrinsic semiconductors with the charge carrier concentration increasing with exactly the same amount as the dopant concentration. Introduction of donor dopants will result in n-type materials, where the number of electrons heavily outnumber the holes. Likewise, for p-type materials having been acceptor doped, the number of holes dominate over the electrons.

2.5 The P-N Junction

The p-n junction is the backbone of semiconductor devices and has been instrumental in the technological advances in the computer industry. The device comprises in all simplicity of n-type and p-type material connected together to form a junction. The types of junctions between n-type and p-type materials can be divided into two main groups, homojunctions and heterojunctions.

2.5.1 Homojunctions

To easily explain the properties of the homojunction, we look at one of the most important p-n junctions in modern history, the Si-based p-n junction. The p-n junction consists of phosphorus doped silicon (n-type), and boron doped silicon (p-type). When doping with B and P, Si atoms are swapped with chemical elements containing a valence electron less and more than silicon respectively. The exchange of elements results in a mobile electron and positively charged immobile phosphorus atom in the n-type, and a mobile electron hole and negatively charged immobile boron atom in the p-type.

Joining the n-type and p-type material, electrons and holes will start to diffuse across the junction. The flow of electrons from the n-type into the p-type material, and the flow of holes from the p-type to the n-type. The immobile charges can't move across the junction and the result is a net positive charge on the n-type and a net negative charge on the p-side. The two opposing charges create an electric field across the junction that sweeps any free charge carriers across the junction, or in other words repulse any charges to cross [28]. This region is called the depletion region and is the basis of the operation for diodes, solar cells and transistors.

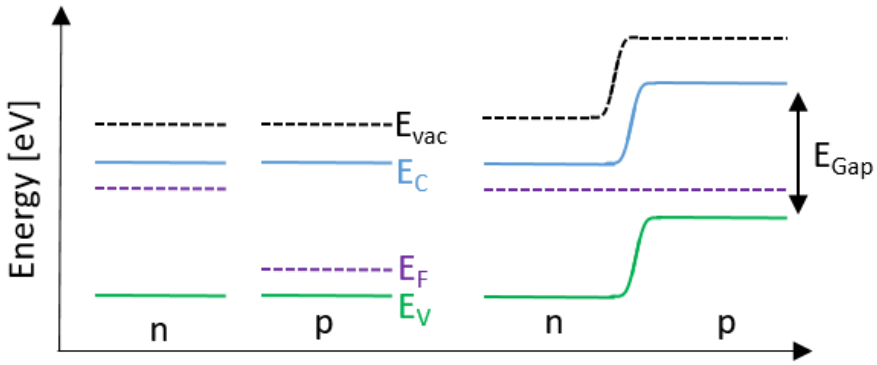

Figure 2-3: Band structure of a n-type and p-type semiconductor, and the p-n junction formed when connected. The difference between the conduction band (E_C) and the valence band (E_V) is the band gap (E_{Gap}). The fermi level (E_F) is constant over the junction, resulting in a band bending across the junction. E_{vac} labels the vacuum level.

Most p-n junctions behave as diodes, meaning that they are rectifying. When a voltage is applied to the p-n junction in such a way that the p-type becomes positive and n-type becomes negative, the holes and electrons are forced towards the junction and recombine

at the interface. The holes and electrons become eliminated, and more electrons and holes can flow into the junction enabling a current to continually flow. However, when the voltage is applied in the opposite direction, there is no elimination at the junction since the electrons and holes are being forced away from the junction. Current is not able to flow, and the p-n junction is said to be rectifying.

2.5.2 Heterojunctions

Heterojunctions are created when two different semiconductor materials are connected. Although the basic working principal of the heterojunction is similar to the homojunction, there are significant differences and different heterojunctions are categorised based on their construction. A general distinction can be made by the material used, such as metal/semiconductor and semiconductor/semiconductor. The first one is commonly known as a Schottky type junction, the latter can also be grouped by the majority charge carrier present, resulting in n-n or p-p type junctions known as “isotype” or n-p type junctions referred to as “anisotype”.

The behaviour of the junction depends on the materials, and three band alignments are possible Figure 2-4. Type I is the most common, where the first semiconductor has a more positive conduction band than the second, and more negative valence band than the second semiconductor. Type II has one semiconductor with a more negative conduction band and a more negative valence band, the other semiconductor with a more positive conduction band and more positive valence band. Type III has one semiconductor with a more positive valence and conduction band, then the other semiconductor, with a more negative conduction and valence band. The flexibility in band alignment makes heterojunctions the basis of complex semiconductor devices such as MOSFETs, tandem solar cells and complex LEDs.

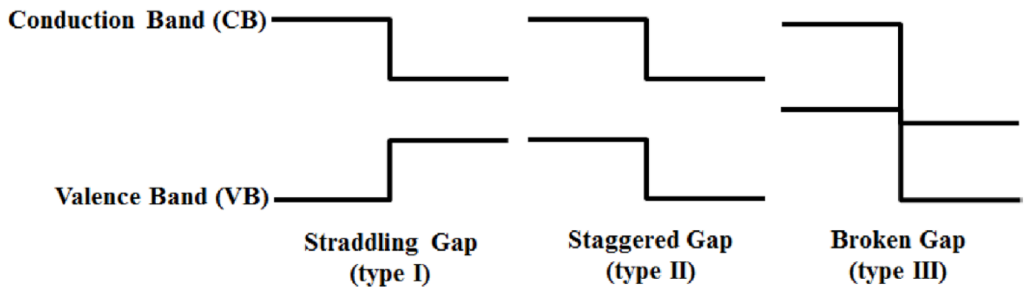

Figure 2-4: Illustration of the three types of band alignment in the most simple heterojunction of two semiconductors. Type I and II can have two different types of band bending depending on the fermi level, while the Type III has only one possibility.[29]

2.6 Thermal Conductivity

Thermal conductivity is the transport of thermal energy from one place to another due to a temperature gradient across the area. The heat can be transported in three different ways, 1. conduction, 2. convection and 3. radiation. Thermal conductivity is how well a material transfers heat by one of these three methods. Heat can also be transported through a material due to an external force, such as described above in Peltier devices as the thermoelectric effect. Under steady state conditions heat transport follows Fourier's law of heat conduction, and can be expressed as

$$q = -k\nabla T \qquad \textit{Eq. 2.13}$$

with q being the heat flux, k is the thermal conductivity and ∇T is the temperature gradient. The negative sign is a result of the heat flow going in the direction of the decreasing temperature. Heat conduction takes contributions from a range of different sources such as, motion of charge carriers, transfer between vibrating atoms, electronic waves or other excitations. The total heat conduction will therefore be the sum of all of its different components.

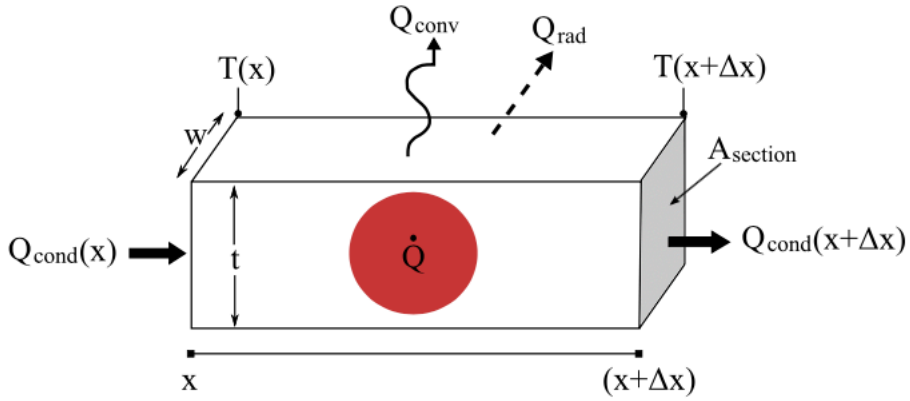

Figure 2-5: Illustration of heat transfer through a solid of length Δx. Q_{cond} is the conduction, Q_{conv} will be its convection and Q_{rad} its radiation.[30]

[

Different materials have large variety in magnitude and temperature dependency mainly due to atomic structure, defects, grain size and lattice forces. Some, tendencies are recognizable, allowing us to divide materials into three categories, metals, semiconductors and insulators. In metals with very high charge carrier count the thermal conduction is mainly the result of the motion of electrons. Even though the motion of these electrons is random, the excess energy of electrons will propagate through the material as thermal energy, from the resulting collisions between them. In semiconductors and insulators, the low concentration of charge carriers results in low thermal conduction by collisions, and the main source of transportation is by lattice vibrations.

3 Literature

3.1 Thermoelectric oxides

3.1.1 Calcium Manganite, $CaMnO_3$

Different perovskites with the general formula ABO_3 have been investigated in the past for thermoelectric properties. Calcium manganite is one such perovskite that has been found to be a n-type thermoelectric material, although it shows low conductivity un-doped (>0.1 Ω cm) [23], electron-doped $CaMnO_3$ is one of the most prominent n-type thermoelectric oxides, because of a high Seebeck coefficient and relative low thermal conductivity [24].

$CaMnO_3$ has an orthorhombic structure at room temperature, with a phase transition at ~896 °C into a tetragonal phase, and a cubic phase above ~913 °C , although the phase transition temperatures are strongly dependant on oxygen stoichiometry [31]. As the undoped material has generally a low conductivity, many reports have been made on increasing its thermoelectric properties. $CaMnO_3$ is usually doped on either the A-site or the B-site, but the highest efficiency values of zT are shown with co-doping of the material. Reports of undoped $CaMnO_3$ has found zT = 0.05 and zT = 0.06 by Flahaut *et al.* [32] and Zhu *et al.* [33] respectively, at temperatures around 800 °C. Theil *et al*. [23] reported a high zT = 0.15 for undoped $CaMnO_3$, however compared to co-doping, Zhu *et al.* [33] reported an increase of zT = 0.27 for Dy and Yb co-doping, *Flahaut et al.* [32] reported an increase of zT = 0.2 with A-site Yb doping and Theil *et al*. [23] reported a zT of 0.25 with B-site W doping.

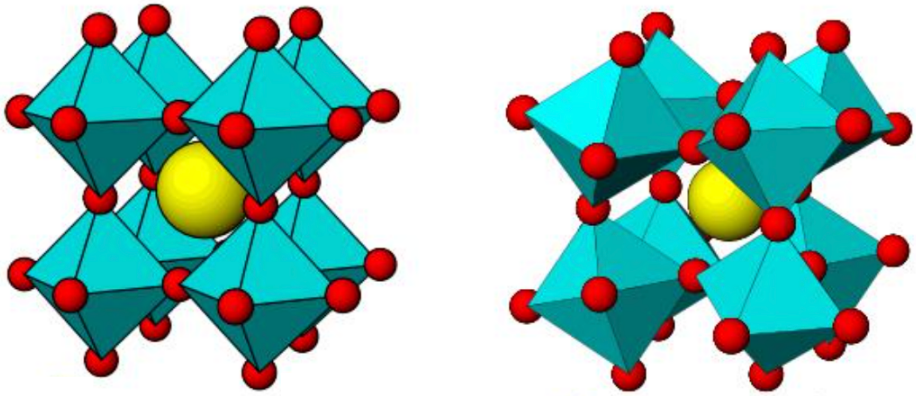

Figure 3-1: Crystal structure of CaMnO3, with large calcium ions (yellow), and manganese in octahedral coordination (teal), oxygen atoms are in red. Left) Cubic phase of CaMnO3 with linear Mn-O-Mn bonds. Right) orthorhombic structure of CaMnO3 with bent Mn-O-Mn bonds.[34]

$CaMnO_3$ has shown a wide variety of oxygen content in different atmospheres, and also having significant increase of oxygen vacancies when the material is heated in air [35, 36]. Goldyreva *et al*. [37] proposed the defect chemistry of $CaMnO_{3\pm\delta}$, showing an increase in electrical conductivity from the charge compensation of oxygen vacancies at high temperatures, contributing electrons to the material and thereby increasing the conductivity.

The defect structure of $CaMnO_3$ has been profoundly studied and two different mechanisms of charge carrier formations have been reported [24, 36-38]. First, there is the formation of oxygen vacancies compensated by localised electrons

$$O^{2-} + 2Mn^{4+} = \frac{1}{2}O_2(g) + v_O + 2Mn^{3+} \qquad \textit{Eq. 3.1}$$

and, secondly there is the intrinsic ionisation by thermal excitation of electrons over the band gap.

$$2Mn^{x}_{Mn} = Mn^{\bullet}_{Mn} + Mn^{/}_{Mn} \qquad \textit{Eq. 3.2}$$

At high temperatures the oxygen exchange reaction (Eq. 3.1) will dominate. The high temperature makes it possible for $CaMnO_3$ to interact with the surrounding atmosphere to create the oxygen vacancies. Below 890 K the oxygen exchange mechanism becomes supressed, and the conductivity is instead dominated by Eq. 3.2, with the temperature activated mechanism of electron generation.

Schrade *et al*. [36] showed significant variations of the electrical conductivity and Seebeck as a result of variations in oxygen non-stoichiometry, explained by small polaron hopping at high temperatures. The activation energy of 0.12 eV to 0.21 eV was reported for oxygen non-stoichiometry ranging from 0.03 to 0.14 respectively.

Lowering the thermal conductivity by increasing the phonon scattering is shown to increase zT, and an investigation by *Singh et al.* [38] of different composites of $CaMnO_3$ showed that an increase of zT=0.05 was achieved with Ruddlesden-Popper phases ($Ca_4Mn_3O_{10}$) zT = 0.06 for Ca rich samples, and a zT = 0.08 for spinel phases ($CaMn_2O_4$) of Mn rich samples.

3.1.2 Calcium Cobaltite, $Ca_3Co_4O_9$

Calcium cobaltite is a misfit layered structure with alternating layers of CoO_2 and intermittent layers of Ca_2CoO_3 [22]. The structure is built of two subsystems, the triple-layered NaCl-type rocksalt CaO-CoO-CaO (Ca_2CoO_3) block (subsystem 1), and a CdI_2-type hexagonal CoO_2 layer (subsystem 2). The subsystems stack along the *c* axis, with a mismatch of the *b* axis between the two subsystems, b_1 = 4.5615 Å and b_2 = 2.8173 Å, with a ratio of 0.62. The structure can therefore be written more precisely as $[Ca_2CoO_3]_{0.62}[CoO_2]$[39].

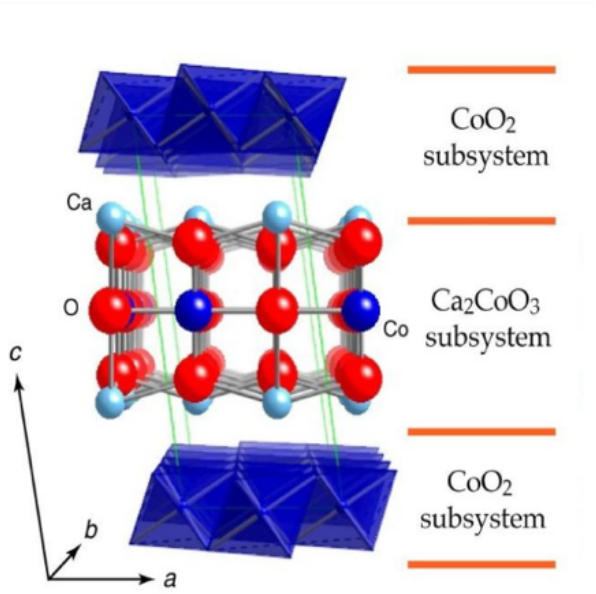

Figure 3-2: Crystal structure of the layered $Ca_3Co_4O_9$. Shown in the figure is the subsystem I of CoO_2 and the subsystem II of Ca2CoO3. Taken from

$Ca_3Co_4O_9$ has been thoroughly investigated and shown to have a consistent electrical conductivity of around 10^4 S m^{-1}, Seebeck coefficient of around 150 μV K^{-1} and thermal conductivity around 2 W K^{-1} m^{-1} at 850 °C [18]. Single crystals of undoped $Ca_3Co_4O_9$ was reported by *Shikano et al.* [40] with a high zT = 0.5 at 800 °C, *Lu et at*. [41] reported a zT=0.15 at 700 °C for polycrystalline samples and a zT = 0.2 was reported by *Wang et al*. [42] at similar temperatures. $Ca_3Co_4O_9$ has also been shown to increase Seebeck and electrical conductivity by doping. The increase in conductivity is attributed to an increase of charge carrier mobility, however a change in microstructure has also been proposed [43]. Ba doped $Ca_3Co_4O_9$ on the A-site was reported by *Lu et at*. [41] with a zT = 0.43 at 700 °C and Eu-doped $Ca_3Co_4O_9$ reported by *Wang et al*. [42] had a zT = 0.3.

The misfit between the lattice of the two subsystems of $Ca_3Co_4O_9$ have been demonstrated to tailor its thermoelectric properties [22] and calculations performed on CCO has shown that the main contribution to the electrical conductivity is due to the CoO_2 subsystem, while the Ca_2CoO_3 subsystem is insulating and is effectively used as a charge reservoir [44]. Cobalt oxides are strongly correlated electron systems, and investigations into the degeneracy of charge carriers and the ratio of the Co^{3+} and Co^{4+} ions was showed to enhance the thermopower [45].

The electronic transport properties of $Ca_3Co_4O_9$ were investigated by Schrade *et al.* [39] establishing a defect model for the different defects present at temperatures between 300 and 875 °C with the influence of oxygen stoichiometry. Two reactions could be observed. Firstly, the formation of holes in the CoO_2 layer and filling of oxygen vacancies in the Ca_2CoO_3 layer

$$v_O^{\bullet\bullet} + \frac{1}{2} O_2(g) = O_O^x + 2h^{\bullet} \qquad \textit{Eq. 3.3}$$

and, secondly the thermally activated formation of an electron-hole pair, the reduction happening in the Ca_2CoO_3 layer and the excitation of the hole in the CoO_2 layer.

$$Co_{Co}^x = Co_{Co}^{/} + h^{\bullet} \qquad \textit{Eq. 3.4}$$

The p-type conductivity therefore stems from intrinsic sources, with the thermally activated holes compensated by the reduction of Co ions in the CoO_2 subsystem. Oxygen vacancies are exclusively formed in the $Ca_2CoO_{3-\delta}$ subsystem up to δ=0.15. Increased conductivity and decreased Seebeck coefficient were reported at an increase in oxygen partial pressure, with the hole concentration ranging from 0.32 to 0.42 per formula. The small polaron transport mechanism was therefore excluded for high temperatures, instead the electronic conduction could be explained by wandering holes. Heikes formula could also not explain the concentration-dependant Seebeck coefficient and was instead related to mobility variation due to the concentration of holes in the material.

3.1.3 $Ca_3Co_{2-x}Mn_xO_6$

Ca_3CoMnO_6 is a compound of the type A_3MXO_6 and has been studied mainly for its interesting magnetic properties from its intrachain interactions. The compound is built up with chains of alternating MnO_6 octahedra and CoO_6 trigonal prisms, surrounded by six chains of calcium antiprisms[46]. It crystallises in a rhombohedral structure and can structurally be classified as a quasi-one-dimensional material. The $Ca_3Co_{2-x}Mn_xO_6$ system can be regarded as $Ca_3Co_2O_6$ with Mn substitution of the B1 site, the amount of manganese (x = 0-1) has been shown to influence the magnetic and electric properties of the material [46]. The interaction between the two transition metal cations Co and Mn dominate the properties of the material. Studies of different compositions has shown that lower amounts of Mn influence the ferromagnetic properties[47], with the stoichiometric x =1 disrupting spin interaction due to the Mn/Co ionic ordering of the system.

A study of the thermoelectric properties by Kanas *et al.*[25] on $Ca_3Co_{2-x}Mn_xO_6$ with different Mn compositions reports that it is a p-type conductor. Charge carrier concentration of holes was directly influenced by the Co concentration on the B1 site at a rate of x – 1. For the x = 1 composition the carrier concentration was found to be solely dependent on thermally generated charge carriers. It is also found that the mobility of holes has the same dependency, with the holes being able to move from Co-Co, but not Mn-Co. The result is the x = 1 composition having thermally generated charge carriers, with very low mobility, giving high Seebeck coefficient, but low conductivity due to low mobility and the highest zT = 0.021 with the x = 0.2 composition.

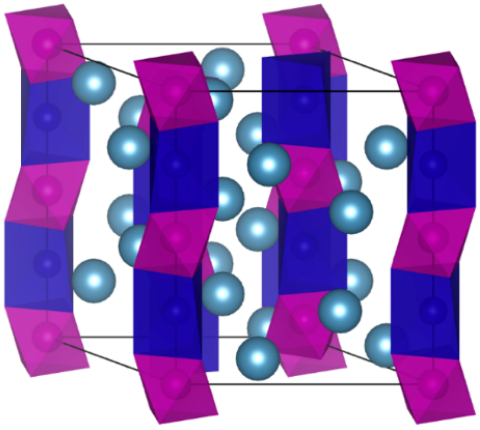

Figure 3-3: Illustration of the crystal structure of Ca_3CoMnO_6. Chains of alternating MnO_6 octahedra (purple) and CoO_6 trigonal prisms (blue) are separated by calcium cations (grey).

3.2 $CaMnO_3$ – $Ca_3Co_4O_9$ Interface

The in-situ formed thermoelectric phase Ca_3CoMnO_6 between the two thermoelectric oxides, $CaMnO_3$ and $Ca_3Co_4O_9$ have been investigated further by Gunnæs *et al.* [48] after its discovery by Kanas *et al.*[25] in an all oxide thermoelectric module with a direct p-n junction. Kanas *et al.*[25] reported a $Ca_3Co_{2-x}Mn_xO_6$ thickness of 5 µm after annealing at 900 °C for 100h. Additionally the layer of $Ca_3Co_4O_9$ showed a 35 µm dense layer at the junction and was found to be Co-rich and Ca-deficient.

Gunnæs *et al.*[48] reported a thin reaction layer of $Ca_3Co_{1+y}Mn_{1-y}O_6$ being formed as a result of Co diffusing into $CaMnO_{3-\delta}$. The reaction layer showed a varied ratio between Co and Mn as seen also by Kanas *et al*. [25] After the formation of the reaction layer the diffusion of more Co was reduced. On the other side, in $Ca_3Co_4O_9$ the Mn diffusion is coupled with Co deficiency creating a decomposition into $Ca_3Co_{1+y}Mn_{1-y}O_6$ and Co-oxide. The increasing layer of $Ca_3Co_{1+y}Mn_{1-y}O_6$ slows the diffusion of Mn and eventually the $Ca_3Co_{1+y}Mn_{1-y}O_6$ formation will stop.

4 Experimental methods

4.1 Preparation

4.1.1 Synthesis of Pellets

The samples investigated in this master thesis were prepared by solid state reaction and the thin films were prepared by pulsed laser deposition (PLD) methods. Three different materials were synthesized, $CaMnO_3$ (CMO), $Ca_3Co_4O_9$ (CCO) and Ca_3CoMnO_6 (CCMO) producing several pellets of CMO, CCO and CCMO to characterize the individual thermoelectric properties, but also investigate the three-layered stack of CMO-CCMO-CCO.

The three different materials were prepared with different temperature treatments and durations that are presented in Table 4-1 below.

Table 4-1:Table of calcination times and temperatures and sintering times and temperatures for all three materials.

Structure formula	1. Calcination temp (°C)	2. Calcination temp (°C)	Calcination time (h)		Sintering temp (°C)	Sintering time (h)
$CaMnO_3$	1050	1050	24	24	1200	20
$Ca_3Co_4O_9$	750	800	12	12	900	24
Ca_3CoMnO_6	1000	1000	10	10	1200	6

All the samples were prepared in the following manner, with different sintering and calcination temperatures and times (Table 4-1). The different synthesis steps; weighing, ball milling, pellet pressing, calcination and sintering are described below.

Weighing. Stoichiometric amounts of the desired precursors for the composition were weighed out with an analytical weight, Sartorius ED224.

Planetary ball milling. The weighed powder was milled in an agate jar together with spherical agate balls and isopropanol. Depending on container size, both 10mm and

15mm agate balls were used, with approximately half the container filled with isopropanol. A Retsch PM100 rotary mill was used at 300 rpm for 2 hours with 15 min intervals. After milling the powder was dried at ~120°C in a Heraeus heating cabinet until the isopropanol had evaporated.

Pellet pressing. The powder was pressed into pellets using a 13mm die and a Specac pellet press, pressed with ~2t.

First calcination. The pellets were calcinated in alumina crucible in a muffled furnace either a Nabertherm LHT 04/17, Nabertherm LV 5/11/P330 or Entech SF-4 at the desired temperature shown in Table 4-1

Second calcination. The pellets were ball milled, dried and calcinated in the same manner as described above. This was done to ensure the full reaction between the precursors and acquire the desired phases composition. The temperature for the second calcination is shown in Table 4-1

Sintering. The powders were pressed into pellets as depicted above and sintered on sacrificial powder in an alumina crucible with an alumina cover. The pellets were sintered as shown in Table 4-1, either in a Nabertherm LHT 04/17 or Entech SF-4.

The precursors used was the same for all samples and are listed in Table 4-2. Ramp rates of the ovens was chosen to be the same for all sampeles, at 5 °C/min up and down in temperature

Table 4-2: Information about the precursors used for the samples prepared by solid-state synthesis

Chemical	Formula	Purity	Supplier
Manganese (IV) oxide	MnO_2	≥99 %	Sigma-Aldrich
Calcium Carbonate	$CaCO_3$	≥99 %	Sigma-Aldrich
Cobalt (II, III) oxide	Co_3O_4	≥99 %	Sigma-Aldrich

Table 4-3: Summary of the samples synthesised during this project. Sample ID, nominal composition, sintering duration and sintering temperature.

Sample ID	Nominal composition	Sintering Duration (h)	Sintering Temperature (°C)
CCMO_Dry	$CaCoMnO_6$	6	1200
CCMO_01	$CaCoMnO_6$	6	1200
CCMO_21	$CaCoMnO_6$	12	1050
CCMO_22	$CaCoMnO_6$	6	1200
CCMO_Target	$CaCoMnO_6$	6	1200
CMO_01	$CaMnO_3$	20	1200
CMO_02	$CaMnO_3$	20	1200
CMO_31	$CaMnO_3$	20	1200
CMO_32	$CaMnO_3$	20	1200
CMO_41	$CaMnO_3$	20	1200
CMO_42	$CaMnO_3$	20	1200
CMO_43	$CaMnO_3$	20	1200
CMO_44	$CaMnO_3$	20	1200
CMO_51	$CaMnO_3$	20	1200
CMO_52	$CaMnO_3$	20	1200
CMO_53	$CaMnO_3$	20	1200
CMO_54	$CaMnO_3$	20	1200
CMO_55	$CaMnO_3$	20	1200
CMO_56	$CaMnO_3$	20	1200
CCO_01	$Ca_4Co_3O_9$	24	920
CCO_02	$Ca_4Co_3O_9$	24	850
CCO_03	$Ca_4Co_3O_9$	24	850
CCO_04	$Ca_4Co_3O_9$	24	850
CCO_51	$Ca_4Co_3O_9$	24	850
CCO_52	$Ca_4Co_3O_9$	24	850
CCO_53	$Ca_4Co_3O_9$	24	850
CCO_54	$Ca_4Co_3O_9$	24	850

4.1.2 Synthesis of Ca_3CoMnO_6 Thin-films

Pulsed laser deposition (PLD) is a form of physical vapour deposition (PVD) technique where a laser beam is used to create the vapor flux for the deposition. PVD uses the generation of a vapour flux from the target material to deposit a thin film on a substrate. In PLD the laser energy is absorbed by the target material, resulting in evaporation, ablation, plasma formation and even exfoliation [49]. The expanding material creates a plume of atoms, molecules, electrons and ions that will condense onto a substrate as a thin film. The process is often done in high vacuum to lower the number of impurities to

the thin film. Atmospheric conditions are regulated depending on what material is being deposited, where reactive gaseous species such as oxygen can be introduced for the deposition of oxides. Since the ablation rate is related to the total mass ablated from the target per laser pulse [50], control over the laser pulse and atmosphere makes PLD ideal for the high production of thin films with complex stoichiometry.

Thin films done by PLD have three growth possibilities, step-flow growth, layer-by-layer growth and three-dimensional growth.

Step-flow growth is observed during depositions on substrates with steps present on its surface or at elevated temperatures.

Layer-by-layer growth, islands continue to nucleate on the surface until a critical island density is reached. As more material is deposited the islands will grow together resulting in a high density of pits on the surface. Additional material will diffuse to these pits and a complete layer will have been formed. This process will then repeat for each subsequent layer.

Three-dimensional growth mode is similar to the second; however, the islands will "stack" on each other, leading to a rough surface since each layer has not been completed.

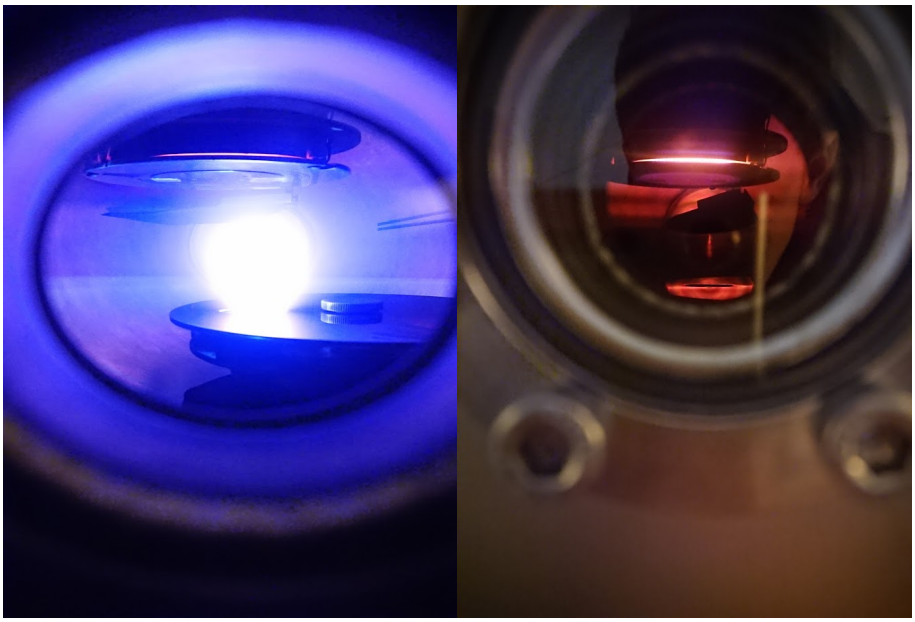

Figure 4-1: Pulsed Laser Deposition done on Ca_3CoMnO_6 target, with $CaMnO_3$ substrates. Left) The bright area is the plume created during the ablation of the target material. Right) Shows the heating of the substrate, for depositions done at 600 °C.

PLD was used to fabricate the CCMO thin films on sapphire substrates and CMO pellets. During the deposition a variety of different parameters can be controlled, and the PLD also has the possibility to adjust mirrors and lenses. The parameters controlled are the distance between target and substrate, number of laser shots, laser intensity, substrate temperature and substrate position. The conditions chosen for the deposition are listed in Table 4-4. The atmosphere chosen during the deposition was chosen to be oxygen, with a pressure of 10^{-3} mbar. The substrate temperature was set to 600 °C for both samples, and a height of 5 cm was chosen.

Table 4-4: Conditions for the PLD synthesis

Target	Laser energy	Atmosphere	Substrate temp	Height
Ca_3CoMnO_6	600 mJ	O_2	600°C	5 cm

The height determines how close the substrate is to the target plume and how uniform the deposited film becomes. Generally, a higher height will result in the deposited thin film becoming more uniform, but the thickness of the film will decrease. With the aim of investigating different CCMO thicknesses on CMO, the height was not altered between the samples with different number of shots. Six thin films were prepared for this thesis, two depositions on Al_2O_3 and four depositions on CMO listed in Table 4-5. The CCMO sample used as the target was CCMO_Target. The sample was polished down after each deposition due to the damage of the surface structure, to avoid uneven deposition of the thin film. The SEM images is shown in appendix C.

Table 4-5: Thin-film samples of Ca_3CoMnO_6 on various substrates.

Substrate	Number of shots	Name Id
Al_2O_3	10 000	Al-01
Al_2O_3	20 000	Al-02
$CaMnO_3$	20 000	CMO-20
$CaMnO_3$	40 000	CMO-40

$CaMnO_3$	60 000	CMO-60
$CaMnO_3$	60 000	CMO-60-01

4.2 Sample Characterisation

4.2.1 Density measurements

Density of all samples was measured with geometric density measurements. The density ρ was found by measuring the height and diameter of the samples with a digital calipher, and the weight on an analytical weight (Sartorius ED2245). The density was then calculated by the equation

$$\rho = \frac{m}{\pi r^2 h} \qquad \textit{Eq. 4.1}$$

here m is the mass in grams, r the radius in cm and h the thickness in cm. The porosity of the samples was calculated by taking the theoretical density ρ_T of the sample and comparing that to the calculated density ρ

$$\phi = \frac{\rho_T - \rho}{\rho_T} * 100\ \% \qquad \textit{Eq. 4.2}$$

4.2.2 X-ray Diffraction

Both intermediate powders and pellets were identified using a D8 Discover by Bruker AXS with a Cu K-alpha 1 radiation and a Ge (111) Johanssen monochromator. Data was collected in the range of 20° - 90° 2θ using Bragg-Brentano geometry, with a step size of 0.02° and 0.1 s/step. The obtained patterns were analysed in DIFFRAC.EVA and the Powder Diffraction File (PDF) by the International Centre for Diffraction Data (ICDD) was used to identify and index the peaks.

4.2.3 Scanning Electron Microscopy

All sintered samples and thin films were investigated by Scanning Electron Microscopy to study the microstructure. Two microscopes were utilized for the SEM images taken in this work.

- **FEI Quanta 200 FEG-ESEM** a microscope with three detectors; an Everhart-Thornley Detector (ETD, a Solid-State Detector (SSD) and an Energy Dispersive X-ray Spectrometer (EDS). The instrument was operated under high-vacuum (10^{-5} Pa) mode with an acceleration voltage of 20 kV.

- **Hitachi SU8230 ultra-high-resolution cold-field emission SEM.** Enabling great signal to noise ratio at low currents over a large range of acceleration voltages (from 0.1 to 30 kV).

Samples were placed on alumina holders, and investigated by either the Everhart Thornley Detector, that detects the secondary electrons and gives information about the topography. Or investigated by the Solid-State Detector, that detects the backscattered electrons and gives information about the phase composition of the sample. The EDS detector was not used in this work.

4.3 Electrical Measurements

4.3.1 Electrical Conductivity and Seebeck Measurement

The electrical conductivity and Seebeck measurements were done with a custom setup in a ProboStat measurement cell, manufactured by NorECs AS, shown in Figure 4-2. The ProboStat was mounted in a vertical tubular furnace that provides the base temperature for the measurement. A Keysight 34970A multichannel multimeter and Keysight E3642A power source was used for the measurements, and to provide current for the integrated resistivity heater. The measurement was controlled and recorded by a custom-built LabVIEW program [51].

The sample was mounted in the ProboStat on the bottom plate, with the thermocouples touching the sample on either side. Four platinum wires were pressed on the sample with springs connected at the base. The temperature of the cell was controlled by the external thermocouple of a wielded Pt-Pt10%Rh type. (Table 4-1). A temperature profile of the measurement is shown in appendix A.

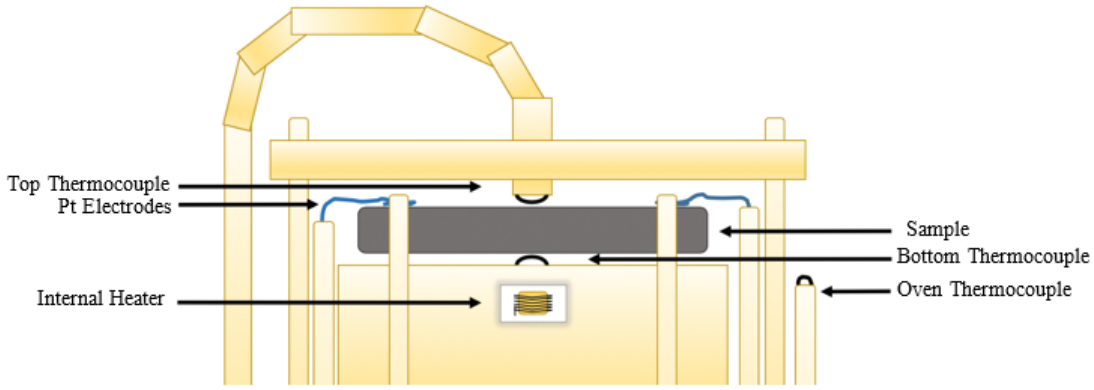

Figure 4-2: Illustration of the setup inside the ProboStat Cell. The sample is held in place with an alumina spring load, that also presses the four electrodes on the sample. The top thermocouple is also spring loaded to have contact with the surface of the sample. An internal heater placed under the bottom thermocouple creates the temperature difference for the Seebeck measurements.

4.3.2 Electrical Conductivity

The electrical resistivity measurements were done by a four-point van der Pauw method. This method gives an average resistivity of the sample and is not limited by how the sample is shaped as long as certain conditions are met. Other benefits of the four-point measurement is that the contact resistance of the sample can be ignored. The conditions for a van der Pauw measurement is that the sample is, 1. A dense sample with no holes or big cracks, 2. Contact point of the electrodes are small and, 3. Sample is uniformly thick, with a height smaller than the surface area.

The measurement was performed by running current through electrode nr. 1 and 2 and measuring the occurring voltage between electrode 3 and 4. The four-point resistance can then be calculated by the equation, $R_{12,34} = \frac{V_{34}}{I_{12}}$. By switching the probes so, the current is run through electrode 3 and 4 and the voltage is measured across 1 and 2, $R_{34,12} =$

$\frac{V_{12}}{I_{34}}$ can be obtained. Several measurements are done with an increasing current I, and the resistance is found by doing a linear fit of the measured points Figure 4-3. The calculated resistances can be inserted in the van der Pauw equation

$$e^{-\frac{\pi R_{12,34}}{R_s}} + e^{-\frac{\pi R_{34,12}}{R_s}} = 1 \qquad \textit{Eq. 4.3}$$

where we find the resistivity is given by the thickness of the sample d.

$$\rho = R_s * d \qquad \textit{Eq. 4.4}$$

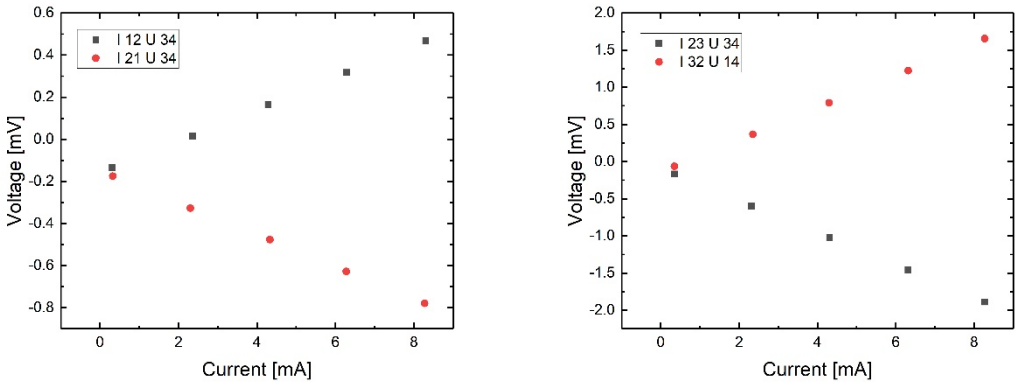

Figure 4-3: Data set obtained from the van der Pauw measurements. The resistance is found from the slope of V/I.

4.3.3 Seebeck coefficient

The Seebeck coefficient is determined by the open circuit voltage ΔU induced on the sample when a heat gradient ΔT is applied.

$$\alpha = \frac{\Delta U}{\Delta T} \qquad \textit{Eq. 4.5}$$

A heat gradient is created over the sample with the heater placed bellow the sample. The current to the heater was set to a maximum current of 450 mA, increased and decreased a total of 13 steps with 0.8 min per step. Measurements of the raw voltage was corrected for the Seebeck coefficient of the Pt-thermocouple, by subtracting the Seebeck coefficient of Pt (Figure 4-4). The corrected voltage could then be plotted against the

temperature difference, and the Seebeck coefficient is the slope of the plot. A typical measurement data set of a Seebeck measurement is shown in appendix A.

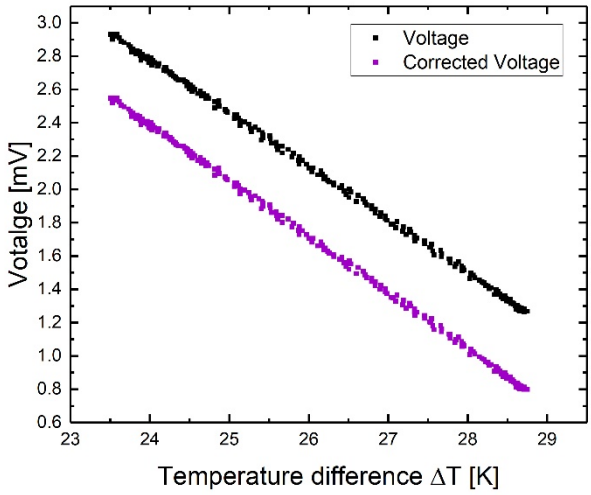

Figure 4-4: Voltage vs temperature difference taken from the data collected from a measurement cycle. The corrected voltage removes the Seebeck coefficient of the Pt-leads. The Seebeck coefficient for the sample is the slope of U vs T of the corrected voltage.

4.4 IV-Current Characteristics

The current voltage characteristics was measured with a four-probe setup on the stack of CMO + CCMO - CMO. Both pellets were painted with Pt paste, and covered with a Pt mesh housing the electrodes, before being placed on top of each other and held down by tension springs in the ProboStat measurement cell Figure 4-5

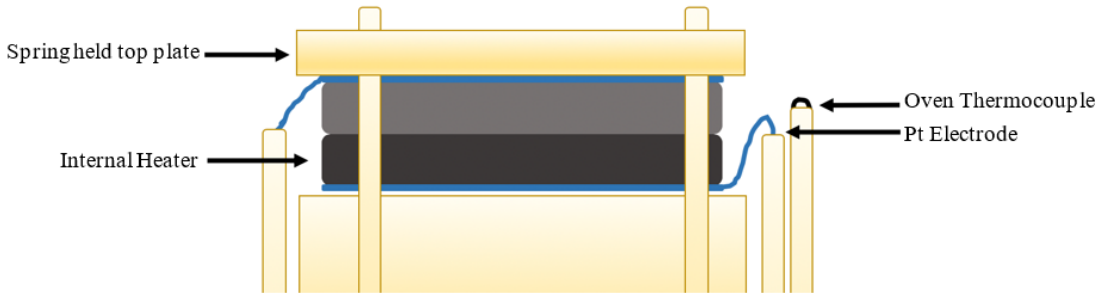

Figure 4-5: Illustration of the experimental setup for the measurement of stacks of CMO and CCO with a CCMO thin-film. The top of each outer surface is painted in Pt paint before adding a Pt mesh connected to the electrodes. The stack is held in place with a spring-loaded alumina top plat. The temperature of the oven is controlled by the external thermocouple

The measurement of the stacks of CMO + CCMO - CCO was performed with a Gamry Reference 3000 instrument. Linear voltammetry sweeps were done from -0.5 V to 0.5 V with a step size of 12 mV. The measurements were performed while the stack was heated from room temperature to 850 degrees, with an oven ramp rate of 2°/min. Measurements of the current-voltage characteristics was done every 30 minutes for the duration of 120 hours for stack 1 and 2, and 50 hours for stack 3 and 4. The resistance was then calculated from the slope of the I-V curves, with linear fitting.

5 Results

5.1 Phase Characterisation

XRD analysis was performed on all three different compositions CCMO, CMO and CCO, and analysis was performed on the phase composition. All the samples show close to phase pure composition. Due to manganese and cobalt present in the materials, scans were taken with reduced background fluorescence.

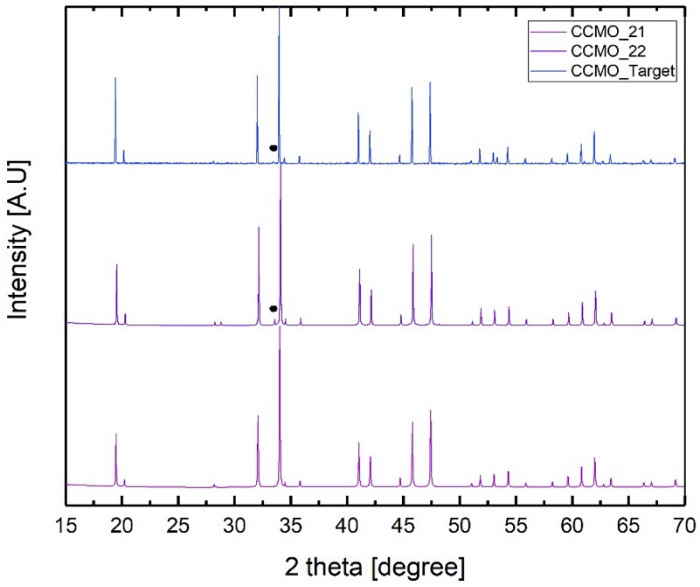

Figure 5-1: The XRD patterns for CCMO samples, CCMO_21 (pink), CCMO_22 (purple) and CCMO_Target (blue). All samples were treated at 1200 °C. All peaks except the one marked as (•) corresponds to the peaks of Ca_3CoMnO_6. The (•) corresponds the peak of Mn_2O_3 but its intensity was very low compared to the others.

The XRD patterns of Ca_3CoMnO_6 show good comparability as is evident from Figure 5-1. All the samples were heat treated in the same manner (1200 °C) and the peak position and intensity corresponds to the reference pattern of Ca_3CoMnO_6. Close to phase-pure composition was obtained, with a very low peak intensity at $2\theta = 33°$ corresponding to the Mn_2O_3 phase. The presence of the Mn_2O_3 phase in CCMO_21 and CCMO_22, but

not CCMO_Target is a result of different stoichiometric variations between the two batches.

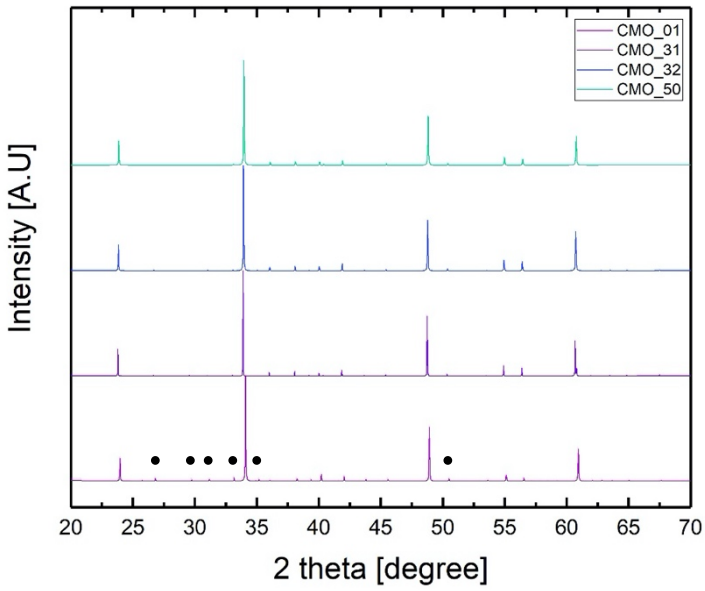

Figure 5-2: The XRD patterns of some of the CMO samples. The CMO samples have all undergone the same heat treatment (1200 °C). CMO_01 (pink), CMO_31(purple), CMO_32 (blue) and CMO_50 (teal). All samples show good comparison to the reference peaks of $CaMnO_3$, except CMO_01 showing low intensity peaks of $CaMn_2O_4$ marked with (•). The CMO_01 pattern is also slightly shifted due to a difference in the holder of the sample.

The XRD patterns of $CaMnO_3$ show good comparability as is evident from Figure 5-2, except for some small intensity peaks identified as the $CaMn_2O_4$ phase. All the samples were heat treated in the same way (1200 °C) and the peak position and intensity correspons to the reference pattern of $CaMnO_3$. Close to phase-pure compositions was obtained, with a very low peak intensity at $2\theta = 52°$ corresponding to the $CaMn_2O_4$ phase. In sample CMO_01 more $CaMn_2O_4$ intensity peaks are present, and indicate a large amount of manganese in the sample.

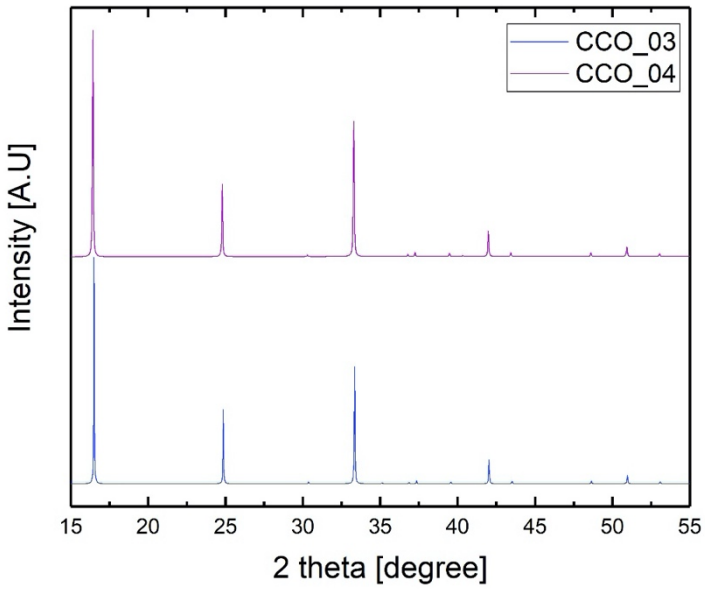

Figure 5-3:The XRD pattern of two of the CCO samples. CCO_03 (blue) and CCO_04 (pink). Both samples were heat treated the same way (850 °C) For both samples all corresponding peaks were identified as $Ca_3Co_4O_9$ in reference to [] , and no other phase composition were identified.

The XRD patterns of $Ca_3Co_4O_9$ show good comparability with each other, as is evident from Figure 5-3. All the samples were heat treated in the same manner at 850 °C. The peak position and intensity correspons to the reference pattern of $Ca_3Co_4O_9$ and no evidence of other phases are present in the diffractogram.

5.2 Microstructure and Morphology

5.2.1 Density

After sintering, samples were weighed and their thickness and diameter measured, to calculate their porosity. The theoretical densities was taken from literature with values given for CCMO, CMO and CCO. For CCMO [25] the theoretical density was given as 4.31 g/cm^3, for CMO [52] the theoretical density was given as 4.58 g/cm^3 and for CCO [53] the theoretical density was given as 4.67 g/cm^3. The measured and calculated values for the samples in the thesis are presented in Table 5-1

Table 5-1: Weight, volume and porosity of the samples presented in this thesis

Sample	Weight (g)	Volume cm^3	Theoretical density g/cm^3	Porosity
CCMO Target	2.243	0.560	4.31	7. %
CCMO_21	0.499	0.128	4.31	10 %
CCMO_22	0.499	0.119	4.31	3 %
CCO_02	0.998	0.312	4.67	32 %
CCO_04	1.010	0.333	4.67	35 %
CCO_51	0.410	0.166	4.67	47 %
CMO_01	1.093	0.268	4.58	11 %
CMO_31	1.010	0.250	4.58	12 %
CMO_32	1.011	0.247	4.58	11 %
CMO_41	0.505	0.124	4.58	11 %

The density calculations show high relative density for the CCMO and CMO samples, but low relative density for the CCO samples. The high porosity of CCO is a result from the complex layered structure, where pressure is needed while sintering to make the structure sinter better. That was however not done in this work, since high density was not a necessity.

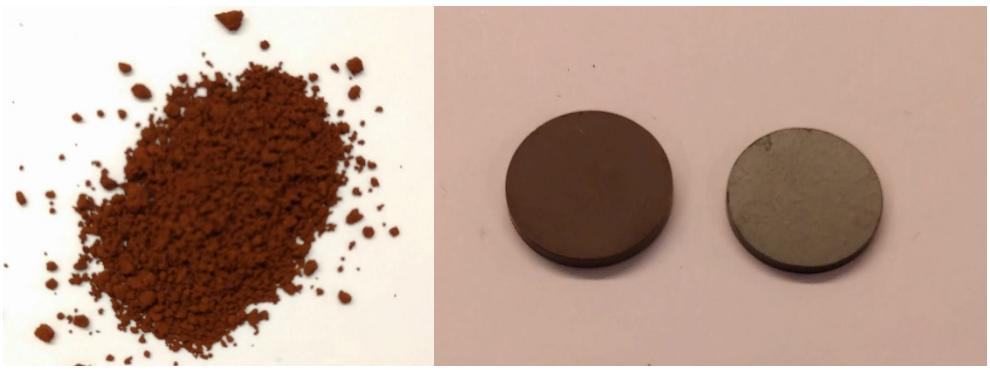

Figure 5-4: Ca_3CoMnO_6 powder to the left and two pellets of Ca_3CoMnO_6 sintered at a) 1050 °C and b) 1200 °C. The colour change from red/brown to grey was observed when Ca_3CoMnO_6 was treated at a higher temperature than 1100 °C.

5.2.2 Surface Morphology and Microstructure

To investigate the surface morphology and microstructure of the samples SEM. The micrographs were acquired using backscattering and secondary electrons detectors (ETD).

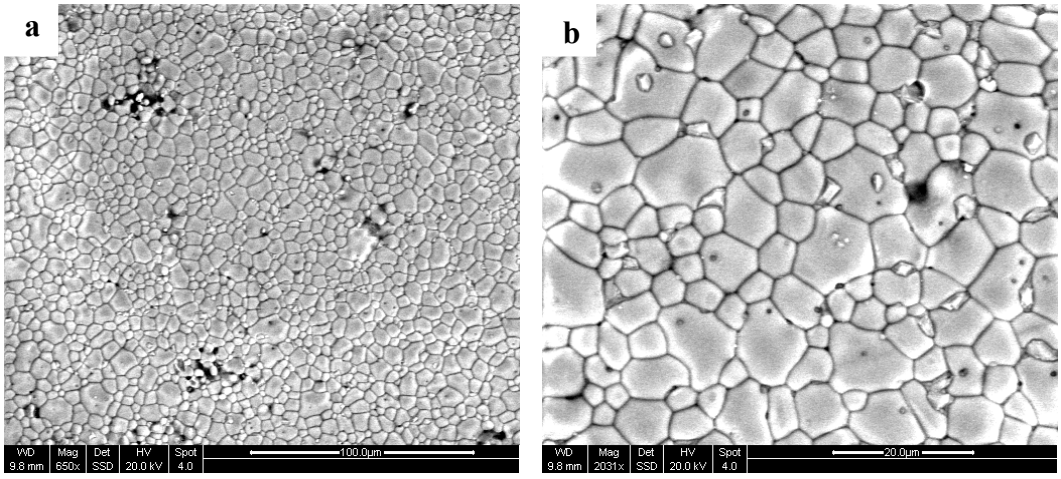

Figure 5-5: SEM images of the surface structure of Ca_3CoMnO_6. Images taken by the SSD imaging. a) Surface structure with the scale shown as 100 µm, giving a clear image of the porosity. b) Surface structure of Ca3CoMnO6 taken at a scale of 20 µm showing a more detailed description of the surface microstructure.

The Ca_3CoMnO_6 micrographs sintered at 1200 °C is shown in Figure 5-5. The surface of the sample appears to have two grain sizes; ~2 µm and ~10 µm. Clear grain boundaries can be observed between the grains, with few pores present in the sample, with good agreement to the low porosity of the sample. Some brighter crystal-like particles are observed on the surface of some grains, and in the grain boundaries.

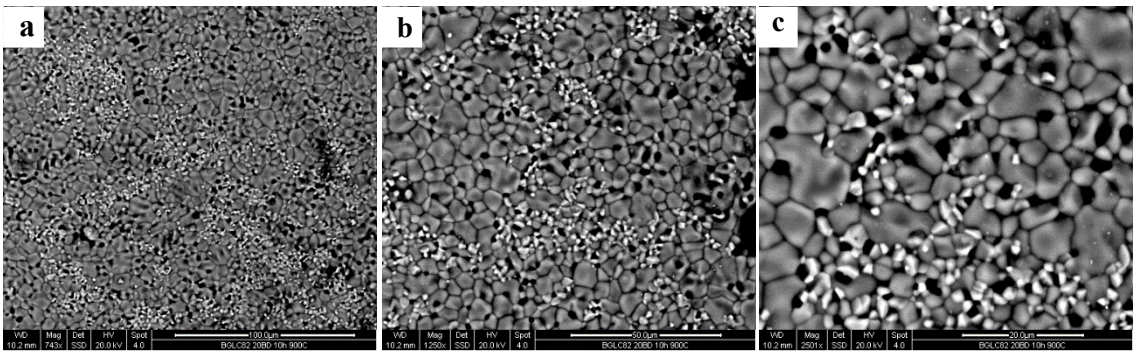

Figure 5-6: SEM images of the surface structure of $CaMnO_3$. Images taken of the SSD imaging. a) Surface structure with the scale set to 100 µm, giving an overview of the sample image. b) Surface structure taken at a scale of 50 µm

showing a more detailed description of the surface microstructure. c) Surface structure taken at a close scale 20 µm to give a clear image of the grains.

The micrographs of $CaMnO_3$ is shown in Figure 5-6. Varying grain size distribution is observed from large grains of 15µm to small grains of 5µm in size. Some of the grains have clear grain boundaries, while others have sintered together. At the triple points of the grain boundaries, darker areas can be observed and corresponds to pores/voids in the sample. These pores are present throughout the sample and are seen clearly in the cross-section of the CMO sample in Figure 5-8.

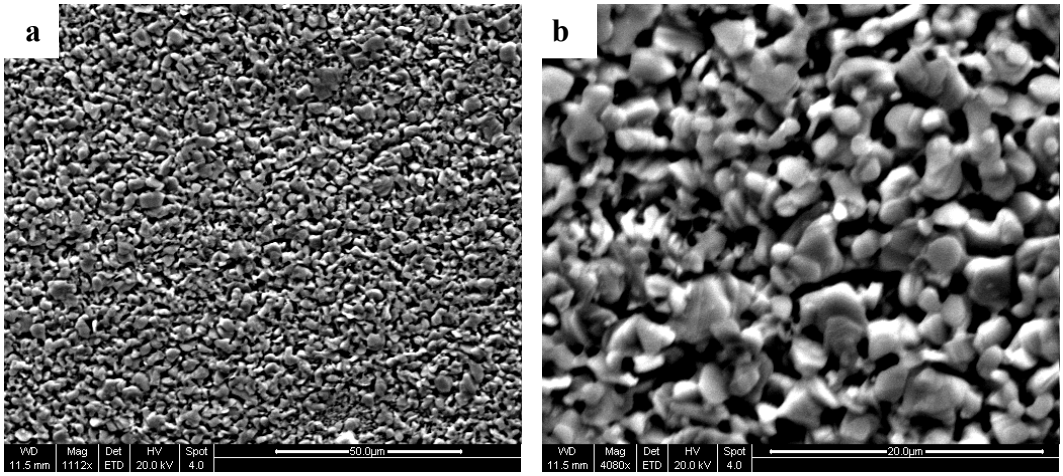

Figure 5-7 SEM images of the surface structure of $Ca_3Co_4O_9$. Images taken of the ETD imaging. a) Surface structure with the scale set to 50 µm, giving an overview of the surface. b) Surface structure taken at a scale of 20 µm showing a more detailed description of the surface microstructure. The porosity of the sample can be observed as the dark areas between the $Ca_3Co_4O_9$

The micrographs of $Ca_3Co_4O_9$ is shown in Figure 5-7. The surface does not resemble a typical layered surface, with a network of sintered grains separated by pores. The sintered grains are around 10µm in size and connected together by thin pillars. There is no decisive orientation of the grains. The large number of pores is in agreement with the density measurements of high porosity observed in the sample. With no pressure on the surfaces during sintering, the typical layered structure does not form to a great extent.

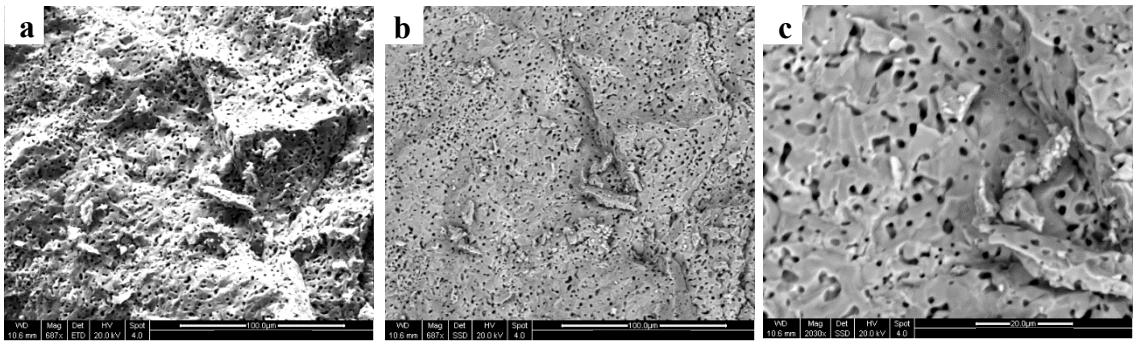

Figure 5-8:SEM images of a fractured $CaMO_3$ pellet, showing the unpolished cross-section. a) Shows the ETD image and b) shows the SSD image of the same area. c) shows a close up image of the surface with the scale of 20 µm. The lighter areas in image a) stem from the scattering of the electrons due to the differences of height on the cross-section. Pores of around 5 µm can be seen clearly in the structure.

The micrographs of the cross-section of a fractured pellet of unpolished $CaMnO_3$ is shown in Figure 5-8. Figure 5-8 a-b) show an overview of the sample, with the brighter areas in image a) stemming from the height differences caused by the fracturing of the pellet and the scattering of the electrons. c) shows the pore structure in the sample, the pores having sizes of around 5 µm evenly distributed in the structure.

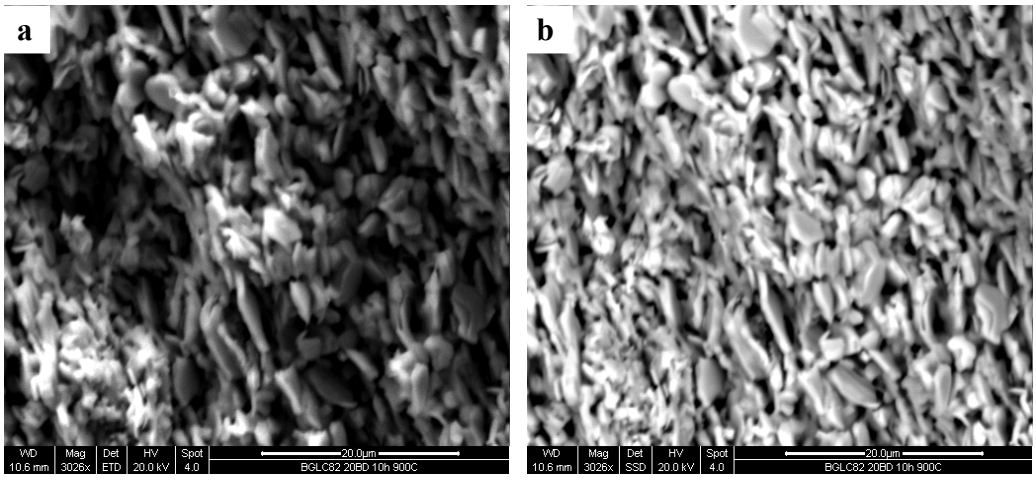

Figure 5-9: SEM images of the cross-section of the fractured $Ca_3Co_4O_9$ pellet. a) Shows the ETD image and b) shows the SSD image of the same area. Darker and lighter areas in image a) show the height differences on the fractured surface. b) shows a clear image of the layered structure, with plates like structures oriented in a similar fashion.

Micrographs of the cross-section of $Ca_3Co_4O_9$ Figure 5-9 shows a more typical layered structure, than the surface (Figure 5-7) with plate like shards of $Ca_3Co_4O_9$ all oriented in a similar orientation throughout the structure. a-b) both show the same area, with the secondary electrons indicating the height difference of the cross-section. Large areas of empty space around the shards contribute to the material having high porosity, as indicated by the density measurements.

Thin-film samples

The microstructure of the thin-films deposited by PLD on Al_2O_3 and $CaMnO_3$ were investigated by using SEM. The thin films deposited on Al_2O_3 were used to determine the growth conditions of Ca_3CoMnO_6, before deposition on $CaMnO_3$. Images of the surfaces were taken prior to the electrical measurements on the stacks of CMO + CCMO-CCO.

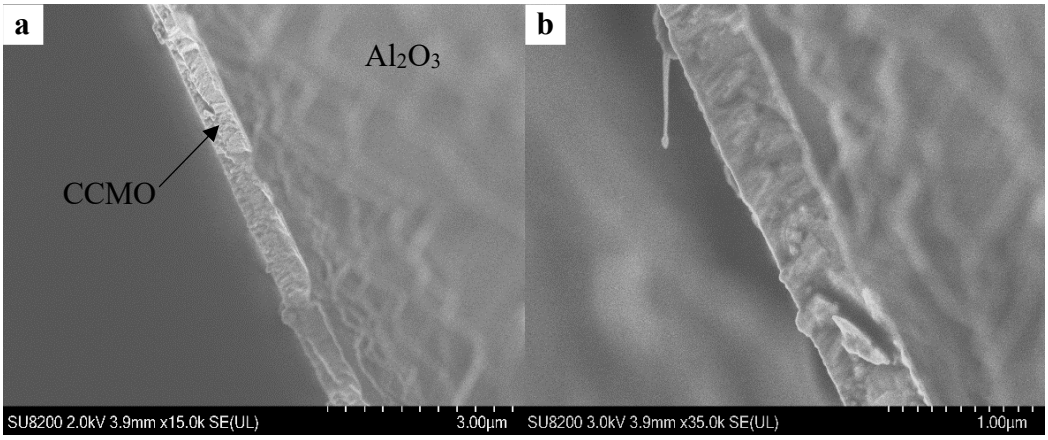

Figure 5-10: SEM image of the Al_01 sample. The sapphire substrate was fractured, and the cross-section observed. The Al_2O_3 substrate can be seen as the rough area to the right on both images a,b). The thin film of CCMO can be clearly seen on both images with a thickness of around 500 nm. Pillars can be observed in the thin film going from the bulk towards the surface as a result from the growth of the film.

For the Al_01 sample, a uniform CCMO thin film can be clearly seen in Figure 5-10 a) and b). The thickness is ca 500 nm, showing a pillar-like grain structure.

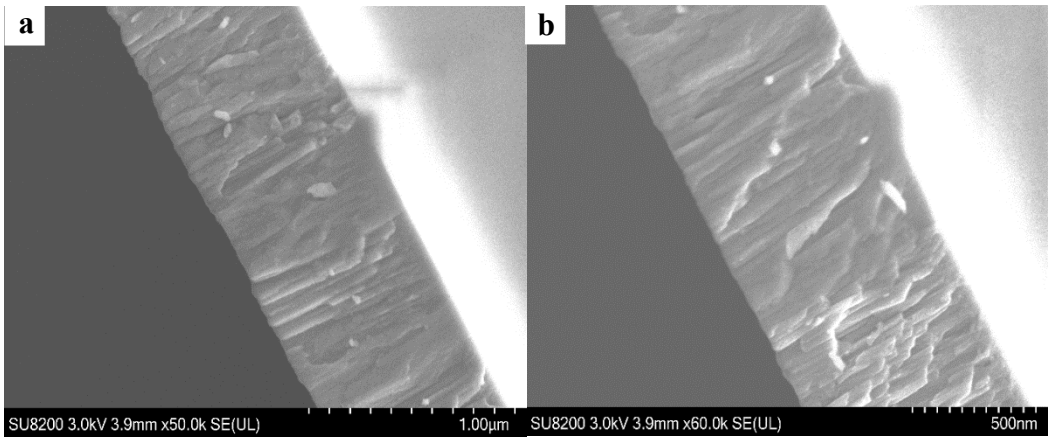

Figure 5-11: SEM image of the Al_02 sample. The sapphire substrate was fractured, and a cross-section of the top layer was observed. The Al_2O_3 substrate can be seen as the light area to the right on both images a,b). The thin film of CCMO can be clearly seen on both images with a thickness of around 750 nm. The light area to the right on both images, is the start of the bulk material Al_2O_3. b) shows the growth of the thin film by the long pillars/rods going from the bulk and outwards.

The Al_02 sample (Figure 5-11) shows a thicker film of CCMO compared to Al_01, as was expected from the increase number of shots. The thickness is around 750 nm. Both Al_01 and Al_02 show uniform growth. The light area on a) and b) is the start of the bulk material Al_2O_3.

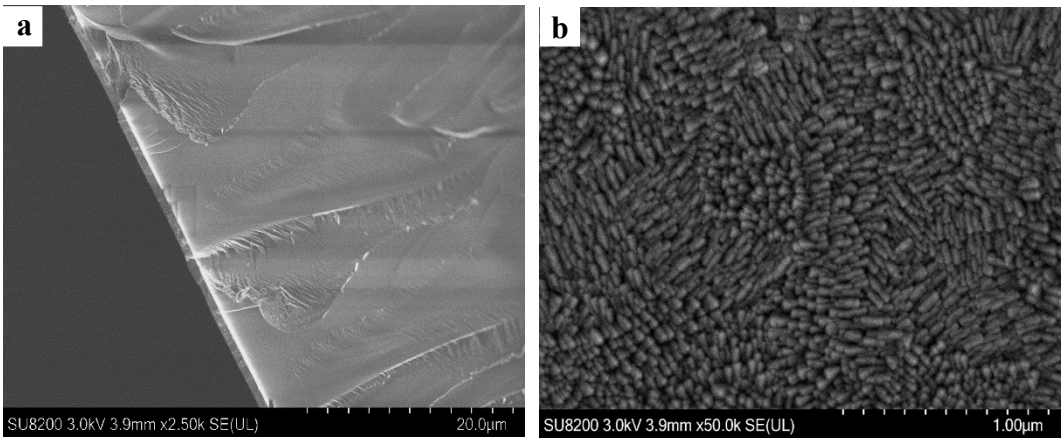

Figure 5-12: a) SEM image of the cross-section of the Al_01 sample, b) SEM image of the surface structure of the Al_01 thin film. a) Bulk Al_2O_3 to the right, with the thin film of CCMO seen as a thin layer before the edge of the sample. Light areas are due to sharp edges on the structure scattering electrons. b) Surface image of the CCMO thin film. Growth of CCMO is seen as pillars, with "domains" of growth in similar directions.

The surface morphology of the Ca_3CoMnO_6 thin film is shown in Figure 5-12, having columns of CCMO growing in different crystal orientations. These clear domains of growth in the same direction indicate that the growth follows the substrate crystal plane until the strain becomes too large and a new growth orientation is started.

The pellets of $CaMnO_3$ were not polished before deposition and the grain boundaries and contours of the uneven surface can be clearly observed in the CMO-20, CMO-40 and CMO-60 samples.

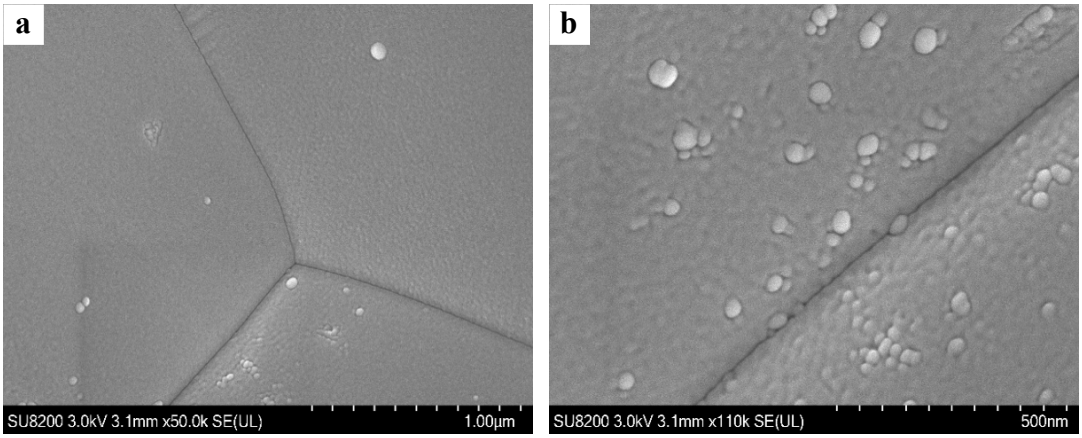

Figure 5-13: SEM images of the surface structure of the CMO_20 sample. a) overview of the surface structure of the sample. The grain boundaries of the $CaMnO_3$ substrate can be clearly seen, with a rough surface indicating the deposition of CCMO. b) is a closer image of the surface, showing the agglomeration of the CCMO on the surface of CMO. The deposition of CCMO is seen to also grow in the grain boundaries.

For CMO-20 with 20 k shots, the growth of Ca_3CoMnO_6 (Figure 5-13) is seen as small bulbs across the sample. Some agglomeration into larger particles of around 50 nm are observed on the surface. a) shows the uniform growth of CCMO, the dark lines representing the grain boundaries of the substrate. Some light large particles are seen on the surface, as the deposited CCMO agglomerates together. b) shows the growth of CCMO also apparent in the grain boundary.

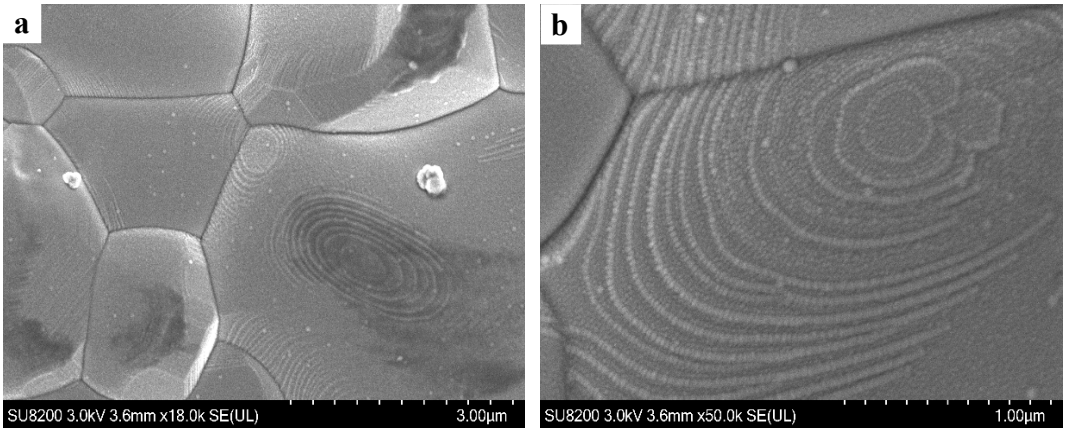

Figure 5-14: SEM images of the surface structure of the CMO_40 sample. a) Overview of the surface structure of the sample. The grain boundaries of the $CaMnO_3$ substrate are indicated by the thick lines on the substrate. b) Closer image of the surface, showing the growth of CCMO on the substrate. "Fingerprints" observed on the surface, as growth of CCMO has not been uniform.

CMO-40 with 40 k shots (Figure 5-14), has similar trends as CMO-20 but with more pronounced bulbs. The grain boundaries are darker, and more pronounced suggesting a thicker thin film. This can also indicate a faster growth on the surface compared to down at the boundaries. There are also "fingerprints" or steps at some areas of the surface where growth of CCMO has not been uniform and could indicate a three-dimensional growth.

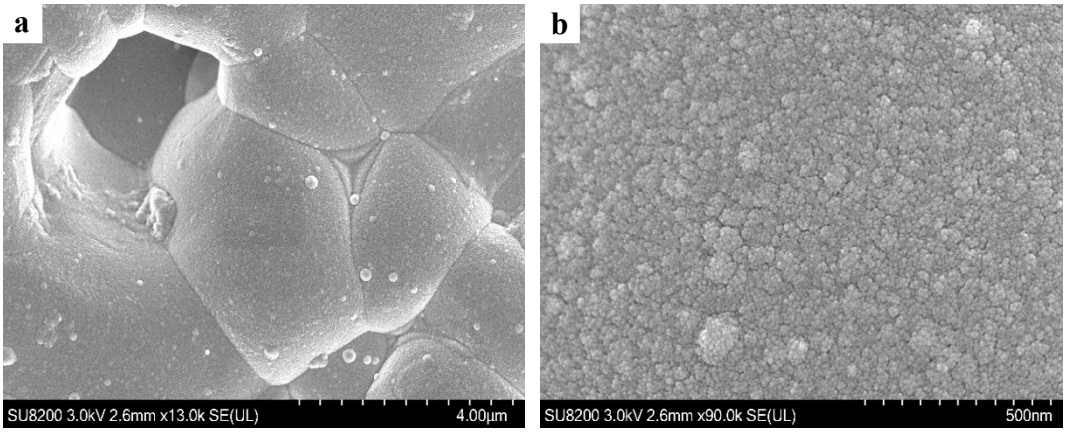

Figure 5-15: SEM images of the surface structure of the CMO_60 sample. a) Overview of the surface of the sample. Voids is shown on the surface due to the sample not being polished before deposition. Agglomeration of some particles can be seen as white bulbs. b) Closer image of the surface, showing the growth of CCMO on the substrate as a many small bulbs, starting to agglomerate.

CMO-60 with 60 k shots (Figure 5-15) the growth of CCMO is similar to the CMO-40, but with larger agglomeration of bulbs creating an even rougher surface than CMO-40 and CMO-20. The grain boundaries also look to be more filled, with more CCMO having been deposited, The growth on all three samples of CMO does not resemble the growth on Al_2O_3.

5.3 Thermoelectric Properties

5.3.1 Electrical Resistivity

The electrical resistivity was measured for the three different materials CCMO, CMO and CCO from 100-850 °C in air. Measurements were taken on the way up, and on the way down in temperature, with 50 °C intervals. The results are presented below for each material.

Ca_3CoMnO_6

Conductivity as a function of temperature is presented for CCMO_22 in (Figure 5-16). A sharp increase in conductivity is seen at around 840 °C. Compared to literature values reported by Kanas *et al*. [25] a conductivity of a factor of 10 lower was shown at 900 °C, dropping in orders of magnitude for lower temperatures. The trend observed for CCMO_22 was closer to the x = 0.75 composition of $Ca_3Co_{2-x}Mn_xO_6$. Due to the high resistivity of the material, measurements at lower temperatures were hard to acquire with the van der Pauw setup.

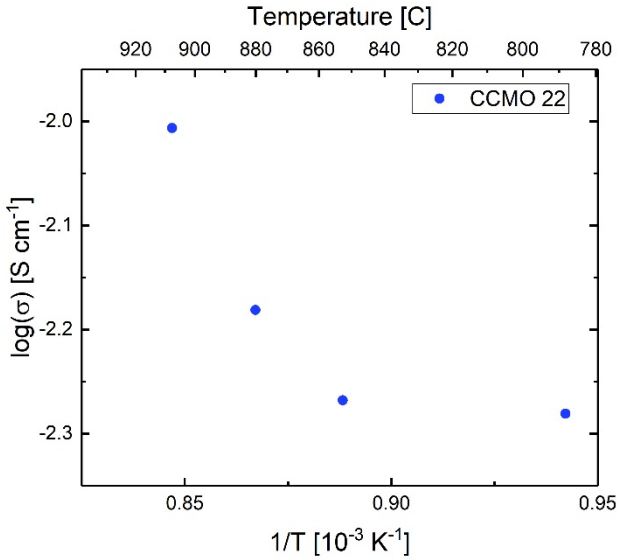

Figure 5-16: Log conductivity vs inverse absolute temperature of CCMO sample CCMO_22 in air.

$CaMnO_3$

Log conductivity vs inverse absolute temperature is shown for CMO_31, CMO_32 and CMO_41 in Figure 5-17. The measurement shows an increase in conductivity from room temperature to 850 °C. For CMO_01 the conductivity is much lower than the CMO_31 and CMO_32 sample at low temperatures. CMO_01 had just one calcination, and could

explain the lower conductivity in the sample. The measured conductivities are in good agreement with literature values for samples CMO_31 and CMO_32.

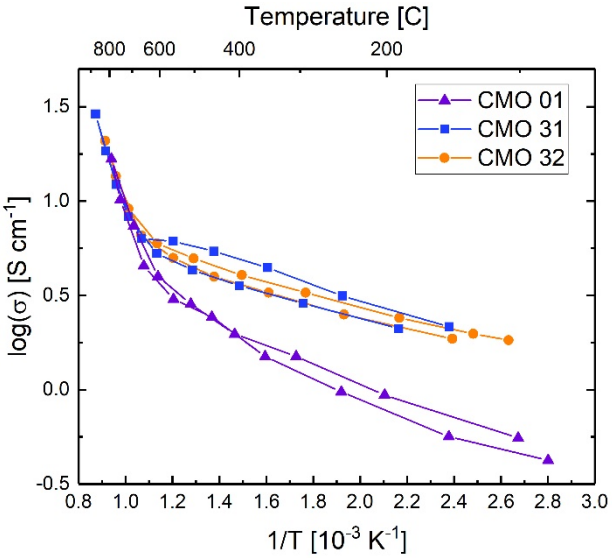

Figure 5-17: Log conductivity vs inverse absolute temperature $CaMnO_3$ samples CMO_31 (blue), CMO_32 (orange) and CMO_01 (purple). CMO_01 was not treated to a second calcination.

Two distinct slopes can be seen in Figure 5-17. Firstly from room temperature to 600 °C and the second from 600 °C to 850 °C. This exponential increase in conductivity, confirms the suggested transport mechanism of small-localised polaron hopping as the dominant transport mechanism. This is also supported by the literature, with the electrons being generated by thermal excitation at lower temperatures and, the formation of oxygen vacancies at high temperatures. To investigate the nature of the conductivity, an Arrhenius type plot of ln(σT) vs 1/T was done of all thee samples, and evaluated through the Arrhenius equation for thermal activation conduction (Eq. 2.5). The two slopes (similar to Figure 5-17) were found by linear regression and the activation energy was calculated to around 0.12 eV at low temperatures and 0.61 eV at high temperatures (Table 5-2).

Table 5-2: Activation energy for the different slopes in sample CMO_01, 31 and 32.

Sample	100-600 °C	600-800 °C
CMO_01	0.10 eV	0.58 eV
CMO_31	0.13 eV	0.62 eV
CMO_32	0.12 eV	0.65 eV

$Ca_3Co_4O_9$

Resistivity vs temperature for the $Ca_3Co_4O_9$ samples CCO_3 and CCO_4 is presented in Figure 5-18 a) and log(σ) vs 1/T is shown in Figure 5-18 b). For the first measurements of both samples, an increase of resistivity was observed between 200 and 500 °C., however where not measured on the way down. Sample CCO_04 was measured a second time (orange), and the resistivity followed the same curve as the first measurement without the increase in the 200 - 500 °C. This could indicate that the CCO was not done sintering, having unreacted phases in the material. The measured conductivities are however around 50 % lower than the reported measurements in literature.

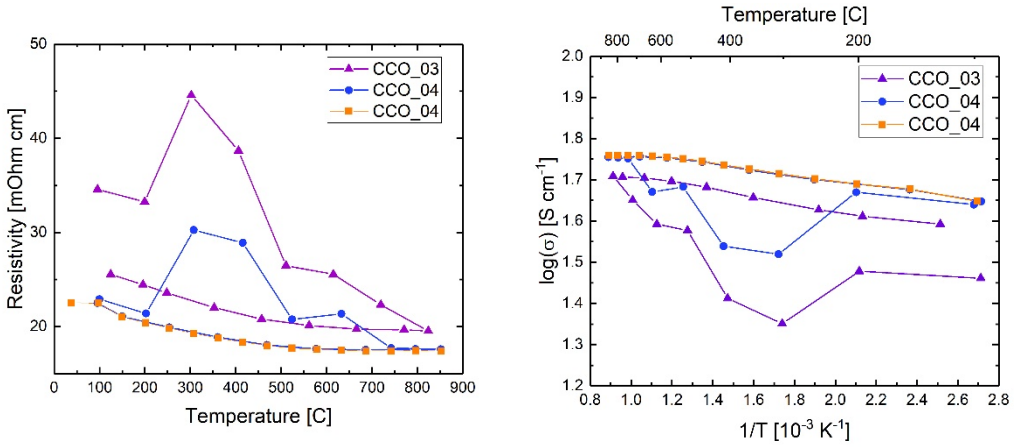

Figure 5-18: The resistivity plotted as a function of temperature for $Ca_3Co_4O_9$ samples CCO_03 (purple) and CCO_04 (blue and yellow)(left), log(σ) plotted as function of 1/T $Ca_3Co_4O_9$ samples CCO_03 (purple) and CCO_04 (blue and yellow) (right). After CCO_04 was measured from 100 – 850 °C (blue) the measurement was preformed again (yellow), and the same curve was following for heating and cooling.

5.3.2 Seebeck coefficient

The Seebeck coefficient of the three different materials were measured simultaneously, as the resistivity measurements in the temperature interval 100-850 °C. The internal

heater was sent a max current of 400 mA, creating the temperature gradient across the sample.

Ca_3CoMnO_6

The Seebeck coefficient as a function of temperature is shown in Figure 5-19 for the CCMO_21 sample. The Seebeck coefficient is shown to be positive, in a range of 50 µV K^{-1} to 300 µV K^{-1} in the temperature range 400 - 850 °C. The positive Seebeck coefficient shows that CCMO is a p-type conductor, consistent with literature [25]. The reported Seebeck coefficient is however much larger at around 500 µV K^{-1} in the same temperature range. The Seebeck values from 400-550 °C could suggest a linear tendency, switching to negative values at lower temperatures, as the majority charge carriers swaps from holes to electrons. The high resistivity of the material make however measuring below 400 °C a challenge with pan ver pauw. All Seebeck measurements done in this work was done cross-plane with the thermocouples placed opposite of each other with the sample in-between, as indicated in the section 3. In-plane measurements of the Seebeck coefficient could potential be better choice for CCMO, and be able to measure the Seebeck coefficient at lower temperatures.

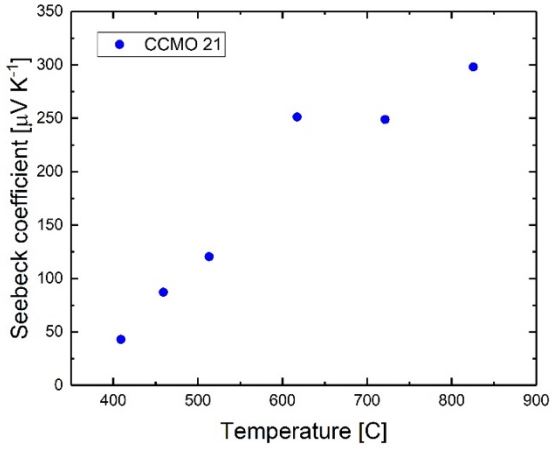

Figure 5-19: Seebeck coefficient vs temperature for Ca_3CoMnO_6 sample CCMO_21.

$CaMnO_3$

The Seebeck coefficient for $CaMnO_3$ samples CMO_01, 31 and 32 are shown in Figure 5-21. The Seebeck coefficient is negative across the whole temperature range indicating electrons as the majority charge carrier in the material, and as such n-type conductivity. Figure 5-21 shows the Seebeck coefficient ranging from -450 to -350 μV K^{-1} at low temperatures (100 °C) for the three samples, and from -250 to -200 μV K^{-1} at high temperatures (850 °C). This is in good agreement with literature for CMO_31, however CMO_01 shows a larger absolute value for the Seebeck coefficient. This could however be explained by CMO_01 having a different phase, such as the Ruddlesden-Popper phase.[non-stoichiometric]

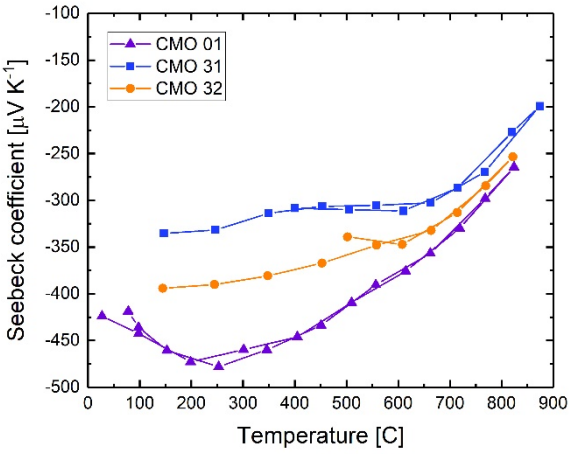

Figure 5-20: Seebeck coefficient vs temperature for $CaMnO_3$ for the different samples CMO_01, CMO_31 and CMO_32.

$Ca_3Co_4O_9$

The Seebeck coefficient is positive indicating holes as the majority charge carrier, and a p-type material. Figure 5-21 shows the Seebeck coefficient increase from around 110 - 125 μV K^{-1} in the temperature range 100-900 °C. The link between the Seebeck coefficient and the conductivity, is shown by the deviation in the same temperature region

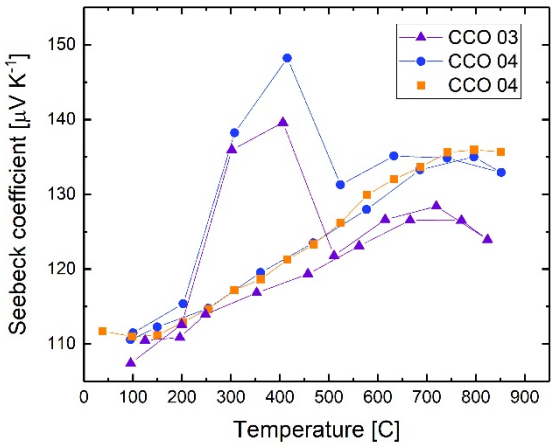

Figure 5-21: Seebeck coefficient vs temperature for $Ca_3Co_4O_9$

5.4 I-V measurements

Four stacks of $CaMnO_3$-$Ca_3Co_4O_9$ were prepared by stacking, two pellets of each respective material on top of each other. To get an understanding of the influence of the insulating thin-film layer of Ca_3CoMnO_6, three stacks of CMO-CCO were created with the CMO thin-film pellets, and one with a CMO pellet with no Ca_3CoMnO_6 thin-film. As recently reported CMO and CCO will react together, and form the $Ca_3Co_{2+x}Mn_xO_6$ composition. Since CCMO is coexisting with both CMO and CCO, no reaction should occur between the two pellets when the thin-film layer is present. The samples used for the stacks are listed in Table 5-3.

Table 5-3: The $CaMnO_3$ and $Ca_3Co_4O_9$ pellets used in the stacks1-4. CMO-60, -40, -20 have had a thin film layer deposited with different amounts of shots of Ca_3CoMnO_6, 60 000, 40 000 and 20 000 respectively.

Sample ID	CMO sample	CCO sample	Time at 850 °C
Stack1	CMO_05	CCO_41	120 h
Stack2	CMO-60	CCO_42	120 h
Stack3	CMO-20	CCO_43	50 h
Stack4	CMO-40	CCO_44	50 h

The resistance calculated from the individual I-V curves vs time is shown in Figure 5-22 for Stack-1. As the stack is heated from room temperature to 850 °C, the resistance across

the whole sample is reduced from 65 Ω to around 0.03 Ω. The resistance steadily increases as the CCMO phase layer is grown at the junction between the two pellets. After around 100 h at 850 °C the resistance has increased from 0.028 Ω to 0.032 Ω. During cooling, the resistance increases to around 3 Ω measured at room temperature. The contact resistance between the Pt electrodes and pellets have not been measured, but can be thought of negligible since the electrodes are stuck on a Pt-mesh, connected with the surface of the samples painted with Pt-paint. The two pellets sticking together after the heat treatment, also confirmed the formation of CCMO at the junction.

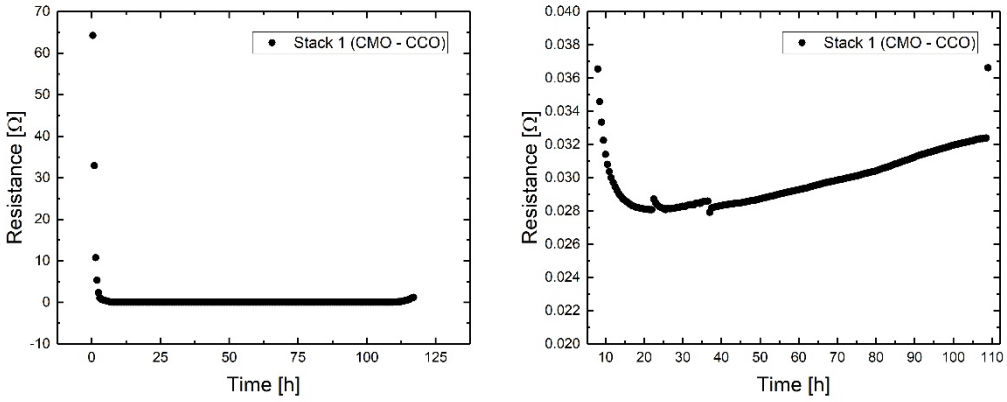

Figure 5-22: Resistance vs time for measurements done on stack 1. Left) Overview plot of the measurement done over 120 hours. Right) Close up of the increase of resistance over time. The stack was left at 850 °C for around 100 h

The individual I-V curves are shown in Figure 5-23 for measurements taken at 20, 70 and 100 hours. The three, current vs voltage curves are linear across the whole temperature duration, with the slopes decreasing so slightly with time. The results show a linear and ohmic tendency for all three curves, that is consistent with the findings of the CMO-CCMO-CCO junction in literature.

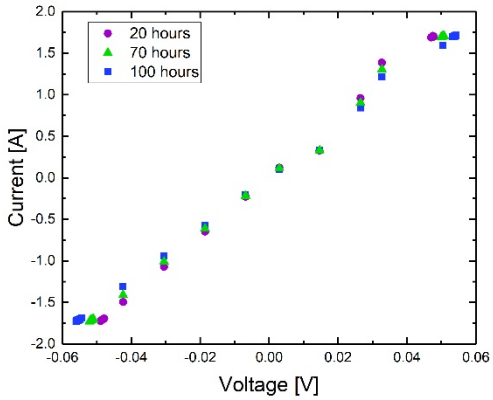

Figure 5-23: I-V curves for stack 1 at 850 °C after 20, 70 and 100 hours. The plot shows omich something in the whole range.

For the stack of CMO-CCO with the thickest thin-film layer of CCMO, Stack-2 the resistance as a function of time is shown in Figure 5-24. At an increase of temperature from room temperature to 850 °C the resistance drops from 250 Ω to around 3 Ω. The increase in temperature after 120 hours at 850 Ω, shows an increase in resistance from 0.3 Ω to around 40 Ω.

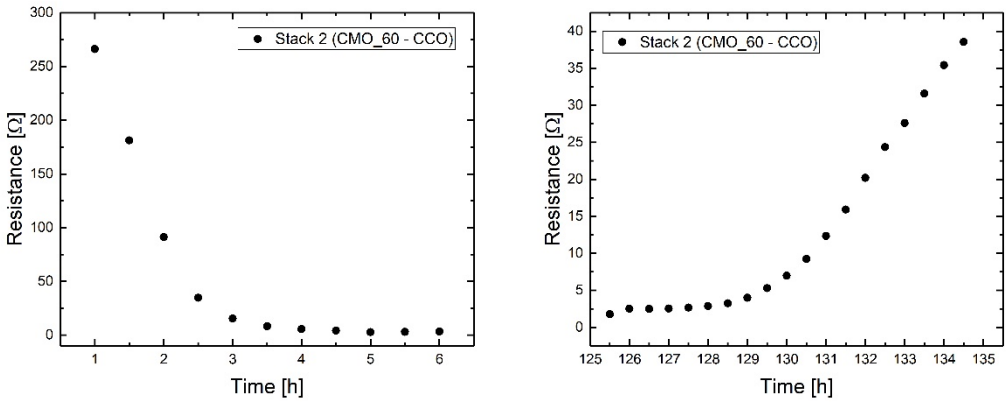

Figure 5-24: Resistance vs time for Stack 2, with the 60 000 shot thin-film between the CaMnO3 layer and Ca3Co4O9 layer. Left) Resistance measured during heating, from room temperature to 850 °C showing a decrease in resistance from 250 Ω to around 3 Ω. Right) Resistance shown during cooling, from 850 °C to room temperature after 120 hours at 850 °C.

The individual I-V curves measured of Stack-2 is presented in Figure 5-25, taken after 30 hours, 118 hours and 125 hours. The measurements show two different curves, one linear and one curved. The I-V curve shows more stable linear behaviour after some hours at 850 °C, and could stem from the thin-film layer forming a better junction with the CCO.

During cooling, the linear slope changes to a more curved I-V dependency. The failed ohmic characteristic make the resistance calculations more inaccurate during cooling.

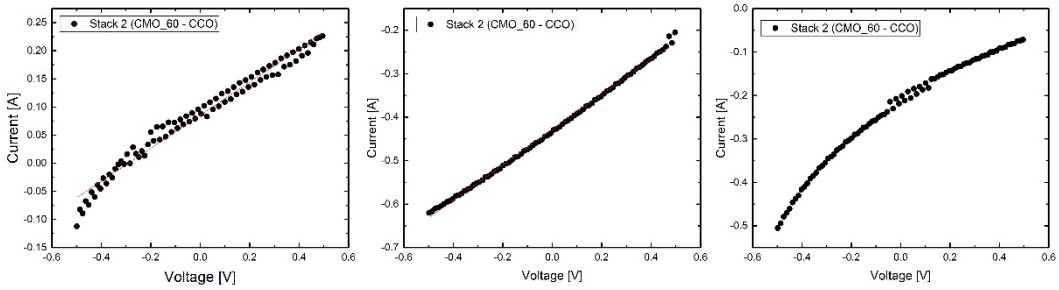

Figure 5-25: Individual I-V plots of Stack-2 taken at 30 h (left), 118 h (centre) and 125 h (right). The first two measurements (left and centre) was taken at 850 °C, while the I-V to the far right was done during cooling, around 750 °C.

The resistance as a function of time for Stack-3 is shown in Figure 5-26. The stack has the least deposited CCMO thin-film layer between CMO-CCO. Resistance decreases with increasing temperatures, and stabilise around 2.5 Ω at 850 °C. The resistance decreases gradually over time, and after 50 hours measured to be around 2.1 Ω. As the temperature is decreased from 850 °C to room temperature the resistance increases to around 5 Ω.

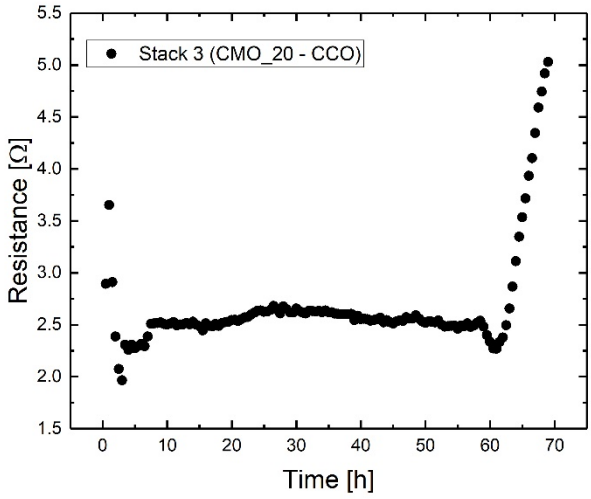

Figure 5-26: Resistance vs time for Stack 3, having the 40 k shot thin film layer of Ca_3CoMnO_6 between the CMO and CCO. The sample was left at 850 °C for around 50 hours.

The individual I-V curves for Stack-3 are presented in Figure 5-27. The I-V measurements are taken after 7, 30 and 60 hours, were all show non-linear dependency.

In all measurements deviations in the current is observed between -0.2 and 0.2 volts. The non-linear tendency also makes the resistances calculated from the slopes inaccurate. The similarity in slopes could however indicate the insulating properties of CCMO, hindering growth more reaction between CMO and CCO.

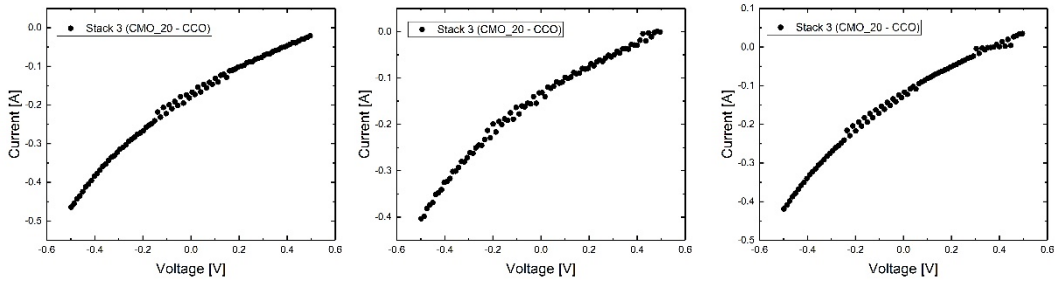

Figure 5-27: Individual I-V measurements of Stack 3, taken at 7 hours (left), 30 hours (centre) and 60 hours (right). Stack 3 was left at 850 °C for a duration of around 50 hours.

Results from resistance vs time for Stack-4 is presented in Figure 5-28. With a deposition of CCMO between Stack-3 and Stack-2 on CMO, the resistance shows simmilar trends to Stack-3. A decrease of resistance from room temperature to 850 °C is observed, stabalizing around 3 Ω at 850 °C. The resistance seems to decrease as the sample is left at 850 °C, and after 50 hours observed around 2.4 Ω. Cooling of the stack, increases the resistance. The stack was left at room temperature for a duration of 10 hours, and the resistance stabailised around 250 Ω.

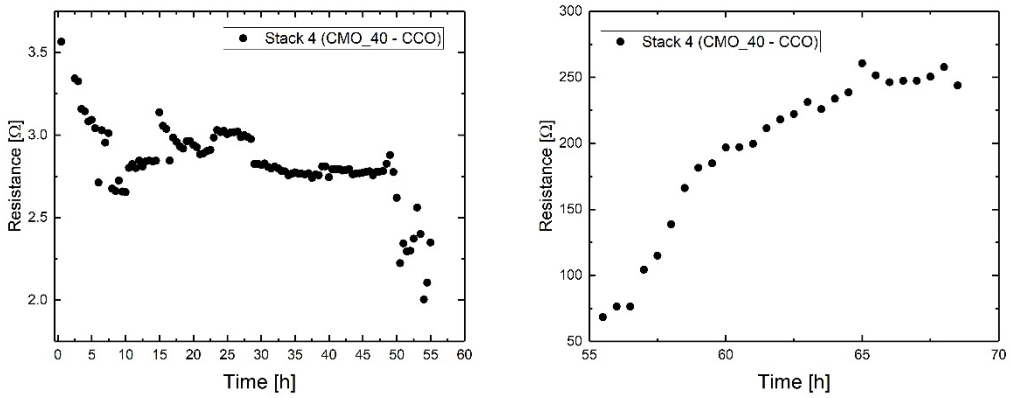

Figure 5-28: Resistance vs time for Stack 4, with the 10 k deposited thin-film between the CMO and CCO. Left) Overview plot of the measurement, Right) Overview plot of the resistance during cooling of the sample from 850 °C to room temperature.

The I-V plots of the individual measurments of Stack-4 is shown in Figure 5-29, after a duration of 10 hours, 30 hours and 50 hours. The plots show more linear characteristics than Stack-3, with small deveations in the slope. The I-V measurment of the stack after 10 hours is more scattered, indicating a better formation of the inerfaces as time increases.

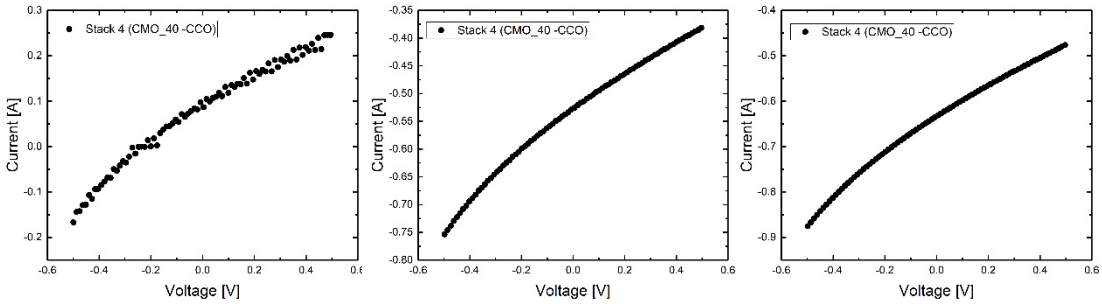

Figure 5-29: Individual I-V curves of Stack 4 for 10 hours (left), 30 hours and 50 hours. More noise in the measurement after 10 hours (left) could indicate a bad interface between the CCMO and CCO

6 Discussion

6.1 $Ca_3Co_{2-x}Mn_xO_6$

$Ca_3Co_{2-x}Mn_xO_6$ of the x = 1 composition was synthesised by solid state reaction. Low intensities peaks identified as Mn_2O_3 was seen in the XRD patterns for CCMO_21 and CCMO_22. Sample CCMO_21 and CCMO_22 showed a change in colour from red to grey Figure 5-4, having been sintered at different temperatures. However, the structural composition seemed similar, when investigated with XRD and under SEM analysis. The observed colour change is therefore most likely an optical effect, stemming from the surface morphology of the samples.

Thermoelectric properties of CCMO was investigated and compared to literature values reported by Kanas et al. [25] The conductivity showed similar values at high temperatures (900 °C) of around 0.01 S cm^{-1}, however at lower temperatures the conductivity measured was orders of magnitude larger than reported for the x = 1 composition. The values reported by Kanas et al. was sintered at lower temperatures (1010 °C), and had a lower relative density. The Seebeck coefficient of 300 μV K^{-1} was around half of what is reported by Kanas et al for the x = 1 composition. The x = 0.75 composition shows more similar results, and could indicate that the CCMO is not fully stoichiometric. No other studies of the thermoelectric properties of CCMO have been found in literature to confirm results.

6.2 $CaMnO_3$

$CaMnO_3$ was synthesises by solid-state reaction, and showed small amounts of the secondary phase $CaMn_2O_4$ if only one calcination was done. The intensities were however gone after the second calcination Surface morphology showed particle sizes of between 15-5 μm, with voids more likely to form at the triple boundaries.

The conductivity measured for $CaMnO_3$ was in good agreement with literature values reported by Schrade *et al.*[36] for high temperature measurements. For the low temperature measurements, the conductivity was found to be lower than reported in literature. The lower conductivity of the CMO_01 sample could indicate another phase in the composition as reported by[38].The electronic transport corresponded to a small polaron mechanism, with an activation energy measured to be around 0.12eV at low temperatures (100-600) and 0.61 eV at higher temperatures. This is in somewhat agreement with literature values of 0.2 eV and 1.0 eV in the two temperature ranges, as shown by Goldyreva *et al*. [37]

Seebeck coefficients of -450 to -200 $\mu V\ K^{-1}$ in the temperature range 100-800 °C was measured, with the CMO_31 sample with best agreement to literature values. The higher absolute value of the Seebeck coefficient for the CMO_01 sample can also be explained by other compositions of $CaMnO_3$. The Seebeck coefficient is mainly affected by charge carrier concentrations, and the oxygen stoichiometry of $CaMnO_3$ has been shown to increase the Seebeck coefficient, by oxygen exchange reactions, and the change of the charge state of Mn^{4+} [36]

6.3 $Ca_3Co_4O_9$

$Ca_3Co_4O_9$ was synthesised by solid-state reaction, however at a low density of around 65 % of the theoretical densities (Table 5-1). Because of its layered structure, samples of CCO require a sintering at high pressures to achieve high relative density. Although, there have been reports of high-density samples made with conventional methods [22]. As the goal of this work was to investigate the CMO-CCO interface, a high density of CCO was no required. The diffractograms showed phase pure compositions, with no secondary phases and a microstructure of typical layered structure (Figure 5-9).

The measured conductivity for $Ca_3Co_4O_9$ was found to be around half of what has been reported in literature [39], and could be attributed to the low density of the sample Seebeck coefficient was found to be around 110-125 $\mu V\ K^{-1}$ in the same temperature range, and is somewhat lower than the reported literature values. Where the transport

mechanism between the two layers in the layered cobaltite, is reason for the high the conductivity and Seebeck coefficient found in the material.

The benefit of the low density would be a lower thermal conductivity; however, measurements of thermal conductivity were not performed in this work. Calculating the zT from reported thermal conductivities in literature gives CCMO a zT = 0.003, CMO a zT = 0.045 and CCO a zT = 0.06, this however is ideal values, and they are still lower than the zT reported for each of the individual materials.

6.4 Ca_3CoMnO_6 Thin-films

Thin-films of CCMO was successfully fabricated on both Al_2O_3 and $CaMnO_3$ by PLD. The growth of CCMO on sapphire showed a homogeneous growth layer of around 500 nm by 10 k shots and 750 nm for 20 k shots. The growth rate of the CCMO is hard to define, since there is only two growth rates, however a linear relationship between the number of shots and thickness of the film can be excluded. The growth on Al_2O_3 also showed a growth pattern following the crystal lattice of the sapphire, with small domains of similar growth with diameters of 4 μm (Figure 5-12).

The growth of CCMO on CMO was also successful, creating a total coverage of the CMO samples. Due to the CMO substrates not being polished before PLD, grain boundaries could be seen clearly on all the samples. However, an agglomeration of larger particles for the 60 k shots compared to the 20 k, indicates a thicker layer of CCMO on CMO. Step like growth observed on the CMO-40 sample, and is most likely a result of the growth of CCMO starting a new layer of growth before the first deposited layers have manage to agglomerate together. [Figure 5-13, Figure 5-14, Figure 5-15]

The thickness of the deposited CCMO thin-film on CMO is hard to analyse since no cross-section of the growth interface was collected, and growth of CCMO on Al_2O_3 does not necessarily transfer onto CMO. Although, the thin-films microstructure shows good indication of an increasing film thickness with number of shots. The coexisting nature of CMO and CCMO shown by Kanas *et al*, and Gunnæs *et al*. [25, 48] would mean a deposited layer of CCMO on CMO would result in a growth of a $Ca_3Co_{2-x}Mn_xO_6$ phase during additional heat treatment. Since the Co and Mn diffusion across the interface

would alter the deposited $Ca_3Co_{2-x}Mn_xO_6$ composition creating a whole gradient of varying stoichiometry.

6.5 Interface of CMO-CCO

To study the benefit of the insulating layer of CCMO between the CMO and CCO material stacks of CMO and CCO were assembled, and their I-V characteristics measured. Expected growth between CMO and CCO was confirmed by the fusion of the two pellets after heat treatment of 100 h at 850 °C, but also the increase in resistance across the stack of CMO and CCO as a function of time, showing an increase from 0.028 Ω to 0.032 Ω. The small increase in resistivity is in good agreement with a thin resistive layer of CCMO forming in the junction as manganese and cobalt atoms diffuses across the junction.. The junction was also found to be ohmic across the 100 hours of growth as reported by Kanas *et al.* for the in-situ grown thermoelectric module, but a much lower resistance was measured across the junction, by a factor of 10^2. This could stem from a lower growth rate of CCMO as the growth by Kanas *et al*. was done at 900 °C and not 850 °C. The CMO and CCO materials were also sintered together by SPS, and not just stacked on top of each other, like here. The resulting junction between the two materials could therefore be considered more "messy" in the stacked setup, and a resulting lower growth rate.

For the stacks of CMO and CCO with the thin film layer of CCMO, two main observations were made. Firstly, the resistance across the junction was much higher for all the stacks compared to the stack of the plain CMO-CCO junction. Secondly the I-V curves did not behave in an ohmic manner, but instead having a slight curved dependency. For the stack with the thickest layer of CCMO, a large decrease in resistance was observed when the temperature increased to 850 °C. With no clear increase or decrease of the resistance, until the temperature was decreased again after 120 hours. The more ohmic I-V properties could be seen as a more coherent junction as CCO "bonds" more tightly with CCMO, as they are coexisting but limit the ability of diffusion.

Stacks 3 and 4 show a negative trend in resistance, decreasing with temperature. This could indicate a formation of more CCMO at the junction, but without the creation of

the cobalt rich, calcium deficient region. The CCMO effectively bridges the two phases together, without the creation of the insulating layer of CoO. The ohmic tendency of the interface seems also dependant on the thickness of the CCMO layer, increasing the ohmic relation with a thicker CCMO layer.

After the measurements were performed, only the pellets with no CCMO layer was held together, and could possibly indicate that the diffusion path for Mn and Co across the CCMO layer is too large. Unfortunately, no time was left to build a thermoelectric module, and compare the thin-film in a direct p-n junction device. Since both CCMO and CCO are p-type conductors, the effect of a directly deposited p-type material on an n-type would be interesting to study.

6.6 Further work

From this study, several areas would benefit on further investigations to get a deeper understanding of the junction and Ca_3CoMnO_6.

- The I-V measurements of the junction was done in quite a hurry due to time constraints, so further investigations of the characteristics of the stacks would be interesting. The trend of increased resistance for the when the reaction layer is being grown, and the decrease or stable resistance for the junctions with the CCMO thin-film would be interesting to take further.

- Create and test a thermoelectric module of the CMO-CCO system with a deposited thin-film layer of CCMO in-between. Since the diffusion of Co and Mn across the junction is vital when the reaction layer is growing the in-situ p-n junction has a large resistance associated with the p-p-n junction, because of the insulating CoO rich phase. Comparing the deposited layer of the p-p-n junction, with the grown could help understand why the increase in power output was shown.

- pO_2 dependencies of the $Ca_3Co_{1-x}Mn_xO_6$ system would be of great interest to get a deeper understanding of the CCMO material under different oxygen

atmospheres, as there is a clear pO_2 dependence of both $CaMnO_3$ and $Ca_3Co_4O_9$ that influences the conductivity and the Seebeck coefficient.

- SEM studies of the interface between $CaMnO_3$ and thin-films of Ca_3CoMnO_6 to find the growth rate of Ca_3CoMnO_6, and if the layer is as uniform as suspected from this work.

7 Conclusion

In this work, the materials Ca_3CoMnO_6, $CaMnO_3$ and $Ca_3Co_4O_9$, the two last being some of the most promising oxide thermoelectric materials has been studied as a direct p-n junction based on the shown device by Kanas *et al.* [25] The main interest was to investigate the p-n characteristics, of the reaction layer and the thin-film layer of CCMO between the two oxide thermoelectric materials CMO and CCO.

Thermoelectric properties

All investigations into the individual thermoelectric properties of the materials showed a generally lower conductivity and Seebeck coefficient compared to literature values for all materials. The $CaMnO_3$ showed a conductivity of 32 S cm^{-1} and Seebeck coefficient of -200 µV K^{-1} at high temperatures. The $Ca_3Co_4O_9$ showed a conductivity of 63 S cm^{-1} and a Seebeck coefficient of 135 µV K^{-1} at high temperatures, and Ca_3CoMnO_6 showed a conductivity of 0.01 S cm^{-1} and Seebeck coefficient of 300 µV K^{-1}

Thin-film growth

Homogeneous thin-films were fabricated on both Al_2O_3 and on $CaMnO_3$. With thicknesses of around 500 nm for 10 k shots at 160 mJ and 750 nm for 20 k shots at 160 mJ. The thin-films grown on $CaMnO_3$ was done on unpolished samples, but gave good adhesion, showing increased growth with the total number of shots. The thickness of the thin-films was unfortunately not measured so growth rates could not be quantized.

P-N junction

The p-n junction between the CMO and CCO was investigated, and compared to the CMO-CCO junction with a thin-film layer of CCMO. The reaction of CMO and CCO was expected creating the $Ca_3Co_{2-x}Mn_xO_6$ interlayer. Showing increased resistance as the thickness of the layer grew. For the CCO-CMO junction with the thin-film layers, the p-n junction behaved also as expected, as the coexisting thin-film layer hindered the formation between CCO and CMO and the junction did not react over time.

8 Bibliography

1. Masson-Delmotte, V., et al., *Global Warming of 1.5°C. An IPCC Special Report on the impacts of global warming of 1.5°C above pre-industrial levels and related global greenhouse gas emission pathways, in the context of strengthening the global response to the threat of climate change, sustainable development, and efforts to eradicate poverty*. 2018, IPCC.

2. Mohtasham, J., *Review Article-Renewable Energies.* Energy Procedia, 2015. **74**: p. 1289-1297.

3. Yin, Y.N., B. Tudu, and A. Tiwari, *Recent advances in oxide thermoelectric materials and modules.* Vacuum, 2017. **146**: p. 356-374.

4. Rodriguez, R., et al., *Review and Trends of Thermoelectric Generator Heat Recovery in Automotive Applications.* IEEE Transactions on Vehicular Technology, 2019. **68**(6): p. 5366-5378.

5. Morelli, D.T., *Thermoelectric Materials*, in *Springer Handbook of Electronic and Photonic Materials*, S. Kasap and P. Capper, Editors. 2017, Springer International Publishing: Cham. p. 1-1.

6. Snyder, G.J. and E.S. Toberer, *Complex thermoelectric materials.* Nat Mater, 2008. **7**(2): p. 105-14.

7. Kim, B., et al., *Phonon manipulation with phononic crystals.* 2012.

8. Bulman, G., et al., *Superlattice-based thin-film thermoelectric modules with high cooling fluxes.* Nat Commun, 2016. **7**: p. 10302.

9. Chen, X., et al., *Thin Film Thermoelectric Materials: Classification, Characterization, and Potential for Wearable Applications.* Coatings, 2018. **8**(7).

10. He, R., G. Schierning, and K. Nielsch, *Thermoelectric Devices: A Review of Devices, Architectures, and Contact Optimization.* Advanced Materials Technologies, 2018. **3**(4).

11. Saini, S., et al., *On-chip thermoelectric module comprised of oxide thin film legs.* Energy Conversion and Management, 2016. **114**: p. 251-257.

12. Becker, A., et al., *A Thermoelectric Generator Concept Using a p-n Junction: Experimental Proof of Principle.* Journal of Electronic Materials, 2013. **42**(7): p. 2297-2300.

13. Kogo, G., et al., *A thin film efficient pn-junction thermoelectric device fabricated by self-align shadow mask.* Sci Rep, 2020. **10**(1): p. 1067.

14. Chen, Z.G., et al., *Nanostructured thermoelectric materials: Current research and future challenge.* Progress in Natural Science-Materials International, 2012. **22**(6): p. 535-549.

15. Chen, W., et al., *Power output and efficiency of a theroelectric generator under temperature control.* Energy Conversion and Management, 2016(127): p. 404-415.

16. Kittel, C., *Introduction to Solid State Physics* 8ed. 2014: John Wiley & Sons, Inc.

17. Flage-Larsen, E. and Ø. Prytz, *The Lorenz function: Its properties at optimum thermoelectric figure-of-merit.* Applied Physics Letters, 2011. **99**(20).

18. Fergus, J.W., *Oxide materials for high temperature thermoelectric energy conversion.* Journal of the European Ceramic Society, 2012. **32**(3): p. 525-540.

19. Michitaka, O., *Recent aspects of oxide thermoelectric materials for power generation from mid-to-high temperature heat source.* Journal of the Ceramic Society of Japan, 2011. **119**: p. 770-775.

20. Karvonen, L., P. Tomes, and A. Weidenkaff, *Thermoelectric Performance of Perovskite-type Oxide Materials.* Material Matters, 2011. **6**: p. 92-99.

21. Terasaki, I., Y. Sasago, and K. Uchinokura, *Large thermoelectric power in NaCo2O4 single crystals.* Physical Review B, 1997. **56**(20): p. R12685-R12687.

22. Madre, M.A., et al., *Preparation of high-performance Ca3Co4O9 thermoelectric ceramics produced by a new two-step method.* Journal of the European Ceramic Society, 2013. **33**(10): p. 1747-1754.

23. Thiel, P., et al., *Influence of tungsten substitution and oxygen deficiency on the thermoelectric properties of CaMnO3−δ.* Journal of Applied Physics, 2013. **114**(24).

24. Funahashi, R., et al., *Thermoelectric properties of CaMnO3 system*, in *2007 26th International Conference on Thermoelectrics*. 2007. p. 124-128.

25. Kanas, N., et al., *All-Oxide Thermoelectric Module with in Situ Formed Non-Rectifying Complex p-p-n Junction and Transverse Thermoelectric Effect.* ACS Omega, 2018. **3**(8): p. 9899-9906.

26. Chevy, F., *Bose Polarons that Strongly Interact.* Physics, 2016. **9**.

27. Tilley, R.J.D., *Understanding solids : the science of materials*. Vol. 2. 2004, Chichester: Wiley.

28. Streetman, B.G. and S.K. Banerjee, *Solid State Electronic Devices*. 2016: Pearson Education Limited.

29. Roul, B., et al., *Binary group III-nitride based heterostructures: band offsets and transport properties.* Journal of Physics D: Applied Physics, 2015. **48**(42).

30. Tecpoyotl-Torres, M., *Polysilicon thermal microactuators for heat scavenging and power conversion.* Journal of Micro/Nanolithography, MEMS, and MOEMS, 2009. **8**(2).

31. Takeuchi, E. and M. Nagao, *High-Temperature Phase Transition of CaMnO3.* 1989.

32. Flahaut, D., et al., *Effect of the Yb substitutions on the thermoelectric properties of CaMnO3.* 2006.

33. Zhu, Y.-H., et al., *Effects of Dy and Yb co-doping on thermoelectric properties of CaMnO3 ceramics.* Ceramics International, 2015. **41**(1): p. 1535-1539.

34. Chemistry, S.S. *Transition Metal Oxide Perovskites*. 2003; Available from: https://www.slideserve.com/Ava/transition-metal-oxide-perovskites-band-structure-electrical-and-magnetic-properties.

35. Bocher, L., et al., *High-temperature stability, structure and thermoelectric properties of CaMn1-xNbxO3CaMn1-xNbxO3 phases.* Acta Materialia, 2009. **57**(19): p. 5667-5680.

36. Schrade, M., et al., *High temperature transport properties of thermoelectric CaMnO3−δ — Indication of strongly interacting small polarons.* Journal of Applied Physics, 2014. **115**(10).

37. Goldyreva, E.I., et al., *Temperature activated electron transport in CaMnO3.* Solid State Ionics, 2014. **262**: p. 678-681.

38. Singh, S.P., et al., *Thermoelectric properties of non-stoichiometric CaMnO3-δ composites formed by redox-activated exsolution.* Journal of the European Ceramic Society, 2019.

39. Schrade, M., et al., *Electronic Transport Properties of [Ca2CoO3−δ]q[CoO2].* The Journal of Physical Chemistry C, 2014. **118**(6): p. 2908-2918.

40. Shikano, M. and R. Funahashi, *Electrical and thermal properties of single-crystalline (Ca2CoO3)0.7CoO2 with a Ca3Co4O9 structure.* Applied Physics Letters, 2003. **82**(12): p. 1851-1853.

41. Lu, Q.M., et al., *Improved Thermoelectric properties of Ca3-xBaxCo4O9 (x=0-0.4). Bulks by Sol-Gel and SPS method.* 2006.

42. Wang, D., et al., *High-temperature thermoelectric properties of Ca3Co4O9+δ with Eu substitution.* Solid State Communications, 2004. **129**(9): p. 615-618.

43. Liu, Y., et al., *Thermoelectric properties of Bi3+ substituted Co-based misfit-layered oxides.* Journal of Electroceramics, 2007. **21**(1-4): p. 748-751.

44. Asahi, R., J. Sugiyama, and T. Tani, *Electronic structure of misfit-layered calcium cobaltite.* Physical Review B, 2002. **66**(15).

45. Koshibae, W., K. Tsutsui, and S. Maekawa, *Thermopower in cobalt oxides.* Physical Review B, 2000. **62**(11): p. 6869-6872.

46. Kaushik, S.D., et al., *Magnetoelectric coupling in Ca3CoMnO6.* Journal of Applied Physics, 2010. **108**(8).

47. Guo, Y.J., et al., *Mean-field theory for ferroelectricity inCa3CoMnO6.* Physical Review B, 2009. **79**(24).

48. Gunnæs, A.E., et al., *Chemical stability of Ca3Co4−xO9+δ/CaMnO3−δ p–n junction for oxide-based thermoelectric generators.* RSC Advances, 2020. **10**(9): p. 5026-5031.

49. Strafe, M., A. Marcu, and N.N. Puscas, *Pulsed Laser Ablation of Solids*. Springer Series in Surface Sciences. 2014.

50. Martín-Palma, R.J. and A. Lakhtakia, *Chapter 15 - Vapor-Deposition Techniques,*. 2013: Elsevier.

51. Schrade, M., et al., *Versatile apparatus for thermoelectric characterization of oxides at high temperatures.* Review of Scientific Instruments, 2014. **85**(10).

52. Materials, S. *CaMnO3 Crystal Structure*. Available from: https://materials.springer.com/isp/crystallographic/docs/sd_0379002.

53. Liou, Y.C., W.C. Tsai, and W.Y. Lin, *Synthesis of Ca3Co4O9 and CuAlO2 Ceramics of the Thermoelectric Application Using A Reaction - Stintering Process.* 2008.

Appendix A

Data collected from a Seebeck coefficient measurement cycle.

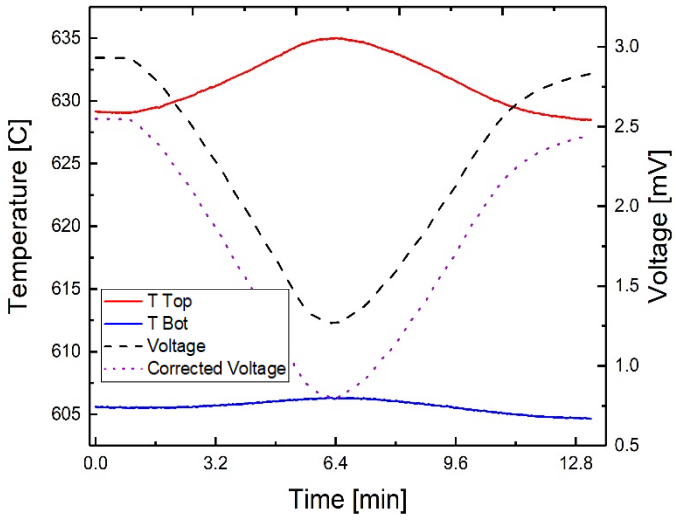

Figure A.1: Data collected from a measurement cycle of the Seebeck coefficient.

Appendix B

Temperature profile for a typical Seebeck and resistivity measurement.

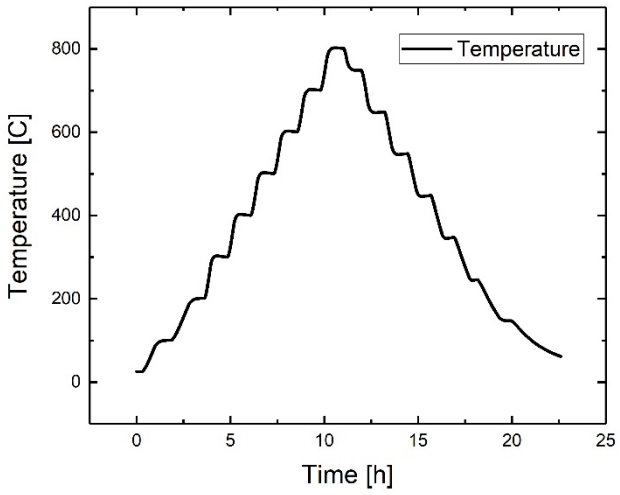

FigureB.1: Temperature profile of the typical measurement cycle for samples of Seebeck and van der Pauw.

Appendix C.

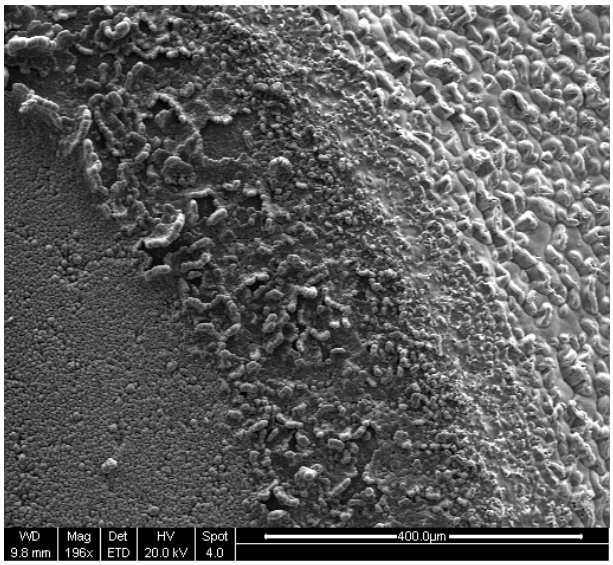

FigureC.1: Surface structure of the CCMO_Target after a deposition of Pulsed laser deposition of CCMO.

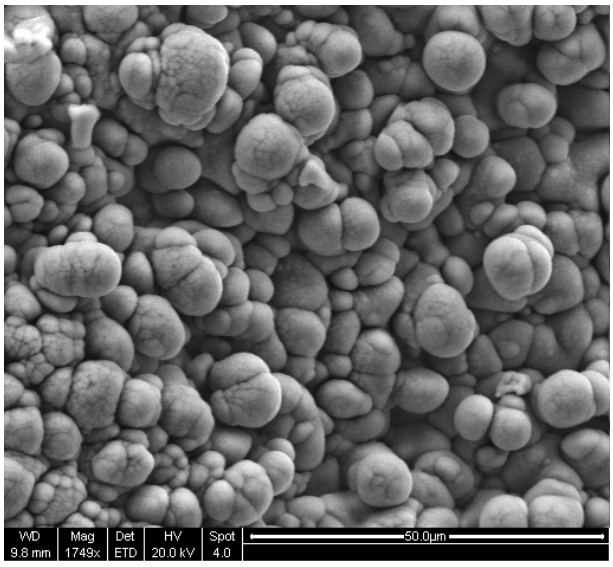

FigureC.2: Close up surface image of the CCMO_Target after PLD deposition